

Full one-loop QCD and electroweak corrections to sfermion pair production in $\gamma\gamma$ collisions *

Xing Li-Rong^b, Ma Wen-Gan^{a,b}, Zhang Ren-You^b, Jiang Yi^b, Han Liang^b, Li Gang^b

^a CCAST (World Laboratory), P.O.Box 8730, Beijing 100080, P.R.China

^b Department of Modern Physics, University of Science and Technology of China (USTC), Hefei, Anhui 230027, P.R.China

Abstract

We have calculated the full one-loop electroweak (EW) and QCD corrections to the third generation scalar-fermion pair production processes $e^+e^- \rightarrow \gamma\gamma \rightarrow \tilde{f}_i\bar{\tilde{f}}_i$ ($f = t, b, \tau$) at an electron-positron linear collider(LC) in the minimal supersymmetric standard model (MSSM). We analyze the dependence of the radiative corrections on the parameters such as the colliding energy \sqrt{s} and the SUSY fundamental parameters A_f , $\tan\beta$, μ , M_{SUSY} and so forth. The numerical results show that the EW corrections to the squark-, stau-pair production processes and QCD corrections to the squark-pair production processes give substantial contributions in some parameter space. The EW relative corrections to squark-pair production processes can be comparable with QCD corrections at high energies. Therefore, these EW and QCD corrections cannot be neglected in precise measurement of sfermion pair productions via $\gamma\gamma$ collision at future linear colliders.

PACS: 12.60.Jv, 14.80.Ly, 12.15.Lk, 12.38.Bx

Keywords: SUSY, QCD correction, electroweak correction, photon collider

*Supported by National Natural Science Foundation of China.

1 Introduction

The standard model (SM) has been successful in describing the strong, weak and electromagnetic interaction phenomena at the energy scale up to 10^2 GeV. At the higher energy scale, it is likely that the minimal supersymmetric standard model (MSSM) is the most attractive candidate among various extensions of the SM. In the MSSM, the existence of scalar partners of all fermions in the SM, namely, two chiral scalar fermions \tilde{f}_L and \tilde{f}_R are required. At future colliders running in TeV energy region, the supersymmetric scalar particle $\tilde{f}\tilde{f}$ pair production processes are very promising channels in probing directly the existence of these scalar fermions, since their production cross sections can be comparatively large, if the scalar fermions are not too heavy.

The two chiral SUSY states \tilde{f}_L and \tilde{f}_R of each fermion f turn to their mass eigenstates by mixing with each other. The mixing size is proportional to the mass of the corresponding SM fermion [1]. Generally, people believe that the sfermions of the third generation are more important in direct SUSY discovery than those of the former two generations, because the sfermions \tilde{f}_L and \tilde{f}_R of the third generation mix strongly to form the two mass eigenstates \tilde{f}_1 and \tilde{f}_2 . We assume that the mass eigenstates $\tilde{f}_1(f = t, b, \tau)$ have lower masses than \tilde{f}_2 . Therefore, \tilde{f}_1 is very probably to be discovered in a relatively lower colliding energy range. Another significance of the sfermion pair production is that it gives access to one of the SUSY fundamental parameters A_f , the trilinear coupling parameter.

The future higher energy e^+e^- linear colliders (LC) is designed to look for the evidences of Higgs boson and other new particles beyond the SM. There have been already some detailed designs of linear colliders, such as NLC[2], JLC[3], TESLA[4] and CLIC[5]. Because of the cleaner background of e^+e^- collision than $pp(\bar{p})$ collision, LC can produce more distinctive experimental signature of new physics. The slepton pair production at LC are intensively discussed in Refs.[6, 7, 8, 9]. The squark pair produced by e^+e^- annihilation has been studied thoroughly, both at tree level and at next-to-leading order[10] [11]. In Ref.[12] the QCD correction to stop pair production via $\gamma\gamma$ fusion at e^+e^- linear collider is investigated. The scalar fermion pair production via e^+e^- collisions $e^+e^- \rightarrow \tilde{f}_i\tilde{f}_j(f = \tau, t, b, i, j = 1, 2)$ at one-loop level, has been studied in detail in [13, 14]. They have considered the complete SUSY-QCD and electroweak (EW) one-loop corrections. Their results show that at the energy of $\sqrt{s} = 500 \sim 1000$ GeV, the QCD corrections are dominated while the EW corrections are of the same magnitude as the SUSY-QCD corrections at the higher energy scale.

However, the future e^+e^- linear colliders are designed to give other facilities operating in e^-e^- , $\gamma\gamma$ and other collision modes at the energy of $500 \sim 5000$ GeV with a luminosity of the order $10^{33}cm^{-2}s^{-1}$ [15]. The future LC's can turn the high energy electron-positron beams into the Compton backscattering energetic photon beams with high efficiency in the scattering of intense laser photons. With the help of the new experimental techniques, it is feasible to yield a scalar fermion pair production directly via the high energy photon collision. Different options of the colliding mode are complementary to each other and will add essential new information to that obtained from the CERN Large Hadron Collider (LHC). Therefore, the sfermion pair production via $\gamma\gamma$ fusion provides another important mechanism in producing sfermion pair. Moreover, their production rates should be larger than those by the e^+e^- annihilation because of the existing of the s-channel suppression in the latter. At the tree-level, the two final sfermions produced in $\gamma\gamma$ collisions should be the same sfermion mass

eigenstate, since only the electromagnetic interaction is involved. Although there are some studies on the $e^+e^- \rightarrow \gamma\gamma \rightarrow \tilde{f}_i \tilde{f}_i$ ($f = t, b, \tau, i = 1, 2$) at tree level[16], the complete one-loop level effects of the EW and QCD in the sfermion pair production via $\gamma\gamma$ collisions are still absent at present. In a word, the process of scalar fermion pair production via photon-photon collisions $e^+e^- \rightarrow \gamma\gamma \rightarrow \tilde{f}_i \tilde{f}_i$ ($f = t, b, \tau, i = 1, 2$) will be worthwhile to investigate precisely and can be accessible in accurate experiments.

In this paper, we will calculate the full one-loop EW and QCD corrections to this process. The paper is organized as follows: In Section 2, we give the definitions of the notations and the analytical calculations of the cross sections involving the $\mathcal{O}(\alpha_{ew})$ EW and $\mathcal{O}(\alpha_s)$ QCD corrections. The numerical results and discussions are presented in Section 3. Finally, we give a short summary in Section 4.

2 Analytical calculations

In this section, we present the analytical calculations for the subprocesses $\gamma\gamma \rightarrow \tilde{f}_i \tilde{f}_i$ ($f = \tau, t, b, i = 1, 2$) and their parent processes $e^+e^- \rightarrow \gamma\gamma \rightarrow \tilde{f}_i \tilde{f}_i$ at the lowest order and the one-loop level in the MSSM. We adopt the 't Hooft-Feynman gauge and the definitions of one-loop integral functions in Ref.[17]. As we know that for the subprocesses $\gamma\gamma \rightarrow \tilde{q}_i \tilde{q}_i$ ($q = t, b, i = 1, 2$) there exist both QCD and EW quantum corrections, while for $\gamma\gamma \rightarrow \tilde{\tau}_i \tilde{\tau}_i$ ($i = 1, 2$) subprocesses they have only EW quantum contributions.

2.1 The sfermion sector and the lowest order cross section of the subprocess $\gamma\gamma \rightarrow \tilde{f}_i \tilde{f}_i$ ($f = \tau, t, b, i = 1, 2$)

In the MSSM, the Lagrangian mass term of the scalar fermion \tilde{f} can be written as

$$-\mathcal{L}_{\tilde{f}}^{mass} = (\tilde{f}_L^* \quad \tilde{f}_R^*) \mathcal{M}_{\tilde{f}}^2 \begin{pmatrix} \tilde{f}_L \\ \tilde{f}_R \end{pmatrix}, \quad (f = \tau, t, b), \quad (2.1)$$

where $\mathcal{M}_{\tilde{f}}^2$ is the mass matrix of \tilde{f} , expressed as

$$\mathcal{M}_{\tilde{f}}^2 = \begin{pmatrix} m_{\tilde{f}_L}^2 & m_f a_f \\ a_f^\dagger m_f & m_{\tilde{f}_R}^2 \end{pmatrix} \quad (2.2)$$

and

$$\begin{aligned} m_{\tilde{f}_L}^2 &= M_{\{\tilde{Q}, \tilde{L}\}}^2 + (I_f^{3L} - Q_f \sin^2 \theta_W) \cos 2\beta m_Z^2 + m_f^2, \\ m_{\tilde{f}_R}^2 &= M_{\{\tilde{U}, \tilde{D}, \tilde{E}\}}^2 + Q_f \sin^2 \theta_W \cos 2\beta m_Z^2 + m_f^2, \\ a_f &= A_f - \mu (\tan \beta)^{-2I_f^{3L}}. \end{aligned} \quad (2.3)$$

where $M_{\tilde{Q}}, M_{\tilde{L}}, M_{\tilde{U}}, M_{\tilde{D}}$ and $M_{\tilde{E}}$ are the soft SUSY breaking masses, I_f^{3L} is the third component of the weak isospin of the fermion, Q_f the electric charge of the scalar fermion, θ_W the Weinberg angle, and A_f is the trilinear scalar coupling parameters of Higgs boson with scalar quarks, μ the higgsino mass parameter.

The mass matrix $\mathcal{M}_{\tilde{f}}$ can be diagonalized by introducing an unitary matrix $\mathcal{R}^{\tilde{f}}$. The mass eigenstates \tilde{f}_1, \tilde{f}_2 are defined as

$$\begin{pmatrix} \tilde{f}_1 \\ \tilde{f}_2 \end{pmatrix} = \mathcal{R}^{\tilde{f}} \begin{pmatrix} \tilde{f}_L \\ \tilde{f}_R \end{pmatrix} = \begin{pmatrix} \cos \theta_{\tilde{f}} & \sin \theta_{\tilde{f}} \\ -\sin \theta_{\tilde{f}} & \cos \theta_{\tilde{f}} \end{pmatrix} \begin{pmatrix} \tilde{f}_L \\ \tilde{f}_R \end{pmatrix} \quad (2.4)$$

Then the mass term of sfermion \tilde{f} can be expressed

$$-\mathcal{L}_{\tilde{f}}^{\text{mass}} = (\tilde{f}_1^* \quad \tilde{f}_2^*) \mathcal{M}_D^{\tilde{f}} \begin{pmatrix} \tilde{f}_1 \\ \tilde{f}_2 \end{pmatrix} \quad (f = \tau, t, b), \quad (2.5)$$

where

$$\mathcal{M}_D^{\tilde{f}} = \mathcal{R}^{\tilde{f}} \mathcal{M}_f^2 \mathcal{R}^{\tilde{f}} \dagger = \begin{pmatrix} m_{\tilde{f}_1}^2 & 0 \\ 0 & m_{\tilde{f}_2}^2 \end{pmatrix}. \quad (2.6)$$

The masses of \tilde{f}_1, \tilde{f}_2 and the angle $\theta_{\tilde{f}}$ are fixed by the following equation

$$(m_{\tilde{f}_1}^2, m_{\tilde{f}_2}^2) = \frac{1}{2} \{ m_{\tilde{f}_L}^2 + m_{\tilde{f}_R}^2 \mp [(m_{\tilde{f}_L}^2 - m_{\tilde{f}_R}^2)^2 + 4|a_f|^2 m_f^2]^{1/2} \}, \quad (2.7)$$

$$\tan 2\theta_{\tilde{f}} = \frac{2|a_f|m_f}{m_{\tilde{f}_L}^2 - m_{\tilde{f}_R}^2} \quad (0 < \theta_f < \pi) \quad (2.8)$$

We denote the subprocess $\gamma\gamma \rightarrow \tilde{f}_i \bar{\tilde{f}}_i$ as

$$\gamma(p_1) + \gamma(p_2) \rightarrow \tilde{f}_i(p_3) + \bar{\tilde{f}}_i(p_4) \quad (f = \tau, t, b, i = 1, 2). \quad (2.9)$$

where p_1 and p_2 represent the four-momenta of the two incoming photons, p_3 and p_4 denote the four-momenta of the outgoing scalar fermion and its anti-particle, respectively. The momenta $p_i (i = 1, \dots, 4)$ obey the on-shell equations, namely, $p_1^2 = p_2^2 = 0$ and $p_3^2 = p_4^2 = m_{\tilde{f}_i}^2$. There are three Feynman diagrams for this subprocess at the tree level, which are shown in Fig.1. The corresponding tree level amplitudes of this subprocess $\gamma\gamma \rightarrow \tilde{f}_i \bar{\tilde{f}}_i$ are represented as

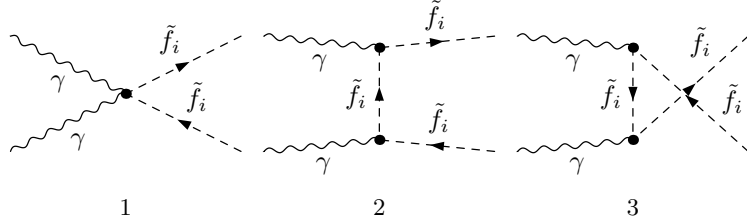


Figure 1: The lowest order diagrams for the $\gamma\gamma \rightarrow \tilde{f}_i \bar{\tilde{f}}_i$ ($f = \tau, t, b$) subprocess.

$$M_0 = M_0^{\hat{t}} + M_0^{\hat{u}} + M_0^{\hat{q}} \quad (2.10)$$

where $M_0^{\hat{t}}$, $M_0^{\hat{u}}$ and $M_0^{\hat{q}}$ represent the amplitudes of the t-channel, u-channel and quartic coupling diagrams respectively. The explicit expressions can be written as

$$M_0^{\hat{t}} = \frac{4ie^2 Q_f^2}{\hat{t} - m_{\tilde{f}_i}^2} \epsilon_\mu(p_1) \epsilon_\nu(p_2) p_3^\mu p_4^\nu, \quad (2.11)$$

$$M_0^{\hat{t}} = M_0^{\hat{t}} (p_1 \leftrightarrow p_2), \quad M_0^{\hat{q}} = 2ie^2 Q_f^2 g^{\mu\nu} \epsilon_\mu(p_1) \epsilon_\nu(p_2). \quad (2.12)$$

The Mandelstam variables \hat{t} , \hat{u} and \hat{s} are defined as $\hat{t} = (p_1 - p_3)^2$, $\hat{u} = (p_1 - p_4)^2$, $\hat{s} = (p_1 + p_2)^2 = (p_3 + p_4)^2$. $m_{\tilde{f}_i}$ ($i = 1, 2$) denotes the masses of the mass eigenstates of scalar fermions.

The cross section at tree-level can be expressed as

$$\hat{\sigma}_0(\hat{s}) = \frac{1}{16\pi\hat{s}^2} \int_{t_{min}}^{t_{max}} dt \bar{\Sigma} |M_0|^2, \quad (2.13)$$

with

$$t_{max,min} = \frac{1}{2} \left[(2m_{\tilde{f}_i}^2 - \hat{s}) \pm \sqrt{(2m_{\tilde{f}_i}^2 - \hat{s})^2 - 4m_{\tilde{f}_i}^4} \right]. \quad (2.14)$$

The summation is taken over the spins and colors of initial and final states, and the bar over the summation recalls averaging over the initial spins. After integration of Eq.(2.13) we get the analytical expressions of the cross section of $\gamma\gamma \rightarrow \tilde{f}_i \tilde{f}_i$ subprocess at the tree level as

$$\hat{\sigma}_0(\hat{s}) = \frac{2\pi\alpha^2}{\hat{s}} Q_f^4 N_C^f \beta \left\{ 1 + \frac{16\mu^4}{1-\beta^2} + \frac{4\mu^2(1-2\mu^2)}{\beta} \log v \right\}. \quad (2.15)$$

Here $\mu^2 = m_{\tilde{f}_i}^2/\hat{s}$ and $\beta = \sqrt{1-4m_{\tilde{f}_i}^2/\hat{s}}$ is the velocity of the produced scalar fermion. The kinematical variable v is defined as $v = (1-\beta)/(1+\beta)$. For squarks, we have $N_C^f = 3$, while for sleptons $N_C^f = 1$.

2.2 $\mathcal{O}(\alpha_{ew})$ EW corrections to subprocess $\gamma\gamma \rightarrow \tilde{f}_i \tilde{f}_i$ ($f = \tau, t, b$, $i = 1, 2$)

In the calculation of the one-loop EW corrections, we adopt the dimensional reduction (\overline{DR}) regularization scheme, which is supersymmetric invariant at least at one-loop level. We assume that there is no quark mixing, i.e., the CKM-matrix is identity matrix, and use the complete on-mass-shell (COMS) renormalization scheme [19]. We use *FeynArts 3* [20] package to generate the $\mathcal{O}(\alpha_{ew})$ Feynman diagrams and amplitudes of the $\mathcal{O}(\alpha_{ew})$ EW virtual contributions to $\gamma\gamma \rightarrow \tilde{f}_i \tilde{f}_i$ ($f = \tau, t, b$) subprocess. There are total 469 EW one-loop Feynman diagrams, and we classified them into four groups: self-energy, vertex, box diagrams and counter-term diagrams. The relevant renormalization constants are defined as

$$\begin{aligned} e_0 &= (1 + \delta Z_e) e, \quad m_{W,0}^2 = m_W^2 + \delta m_W^2, \\ m_{Z,0}^2 &= m_Z^2 + \delta m_Z^2, \quad A_0 = \frac{1}{2} \delta Z_{AZ} Z + (1 + \frac{1}{2} \delta Z_{AA}) A \\ m_{\tilde{f}_i,0}^2 &= m_{\tilde{f}_i}^2 + \delta m_{\tilde{f}_i}^2, \quad \tilde{f}_{1,0} = Z_{11}^{\tilde{f}^{1/2}} \tilde{f}_1 + Z_{12}^{\tilde{f}^{1/2}} \tilde{f}_2, \quad \tilde{f}_{2,0} = Z_{22}^{\tilde{f}^{1/2}} \tilde{f}_2 + Z_{21}^{\tilde{f}^{1/2}} \tilde{f}_1. \end{aligned} \quad (2.16)$$

where

$$Z_{ij}^{\tilde{f}^{1/2}} = \delta_{ij} + \frac{1}{2} \delta Z_{ij}^{\tilde{f}}.$$

With the on-mass-shell conditions, we can obtain the renormalized constants expressed as

$$\delta m_W^2 = \tilde{R}e\Sigma_T^W(m_W^2), \quad \delta m_Z^2 = \tilde{R}e\Sigma_T^{ZZ}(m_Z^2),$$

$$\delta Z_{AA} = -\tilde{Re} \frac{\partial \Sigma_T^{AA}(p^2)}{\partial p^2} \Big|_{p^2=0}, \quad \delta Z_{ZA} = 2 \frac{\tilde{Re} \Sigma_T^{ZA}(0)}{m_Z^2},$$

$$\delta Z_e = -\frac{1}{2} \delta Z_{AA} + \frac{s_W}{c_W} \frac{1}{2} \delta Z_{ZA} = \frac{1}{2} \tilde{Re} \frac{\partial \Sigma_T^{AA}(p^2)}{\partial p^2} \Big|_{p^2=0} + \frac{\sin \theta_W}{\cos \theta_W} \frac{\tilde{Re} \Sigma_T^{ZA}(0)}{m_Z^2}, \quad (2.17)$$

$$\delta m_{\tilde{f}_i}^2 = \tilde{Re} \Sigma_{ii}^{\tilde{f}}(m_{\tilde{f}_i}^2), \quad \delta Z_{ii}^{\tilde{f}} = -\tilde{Re} \frac{\partial \Sigma_{ii}^{\tilde{f}}(p^2)}{\partial p^2} \Big|_{p^2=m_{\tilde{f}_i}^2},$$

$$\delta Z_{ij}^{\tilde{f}} = -\tilde{Re} \frac{2 \Sigma_{ij}^{\tilde{f}}(m_{\tilde{f}_j}^2)}{m_{\tilde{f}_j}^2 - m_{\tilde{f}_i}^2} \quad (i, j = 1, 2 \quad i \neq j). \quad (2.18)$$

\tilde{Re} means taking the real part of the loop integrals appearing in the self-energy. The $\Sigma_{ij}^{\tilde{f}}, (i, j = 1, 2)$ appeared in Eqs.(2.18) denote the unrenormalized sfermion self-energy involving only the EW interactions. The $\mathcal{O}(\alpha_{ew})$ one-loop virtual corrections to $\gamma\gamma \rightarrow \tilde{f}_i \bar{\tilde{f}}_i$ is represented as

$$\Delta \hat{\sigma}_{vir}^{EW} = \hat{\sigma}_0 \hat{\delta}_{vir}^{EW} = \frac{1}{16\pi\hat{s}^2} \int_{\hat{t}_{min}}^{\hat{t}_{max}} d\hat{t} \ 2\tilde{Re} \overline{\sum} (M_{vir}^{EW} M_0^\dagger). \quad (2.19)$$

The expressions of $\hat{t}_{max, min}$ have been presented in Eq.(2.14) and the summation with bar over head represents same operation as that appeared in Eq.(2.13). M_{vir}^{EW} is the renormalized amplitude of the EW one-loop Feynman diagrams, which include self-energy, vertex, box and counter-term diagrams.

The $\mathcal{O}(\alpha_{ew})$ virtual corrections contain both ultraviolet (UV) and infrared (IR) divergences. After renormalization procedure, the UV divergence should vanish. We have checked the cancellation of the UV divergence both analytically and numerically, and confirmed that we got a UV finite amplitude at the $\mathcal{O}(\alpha_{ew})$ order. The IR singularity in the M_{vir}^{EW} is originated from virtual photonic loop correction. It can be cancelled by the contribution of the real photon emission process. We denote the real photon emission as

$$\gamma(p_1) + \gamma(p_2) \rightarrow \tilde{f}_i(p_3) + \bar{\tilde{f}}_i(p_4) + \gamma(k) \quad (f = \tau, t, b, \ i = 1, 2), \quad (2.20)$$

where $k = (k^0, \vec{k})$ is the four momentum of the radiated photon, and p_1, p_2, p_3, p_4 are the four momenta of two initial photons and final state particles $\tilde{f}_i \bar{\tilde{f}}_i$, respectively. The real photon emission Feynman diagrams for the process $\gamma\gamma \rightarrow \tilde{f}_i \bar{\tilde{f}}_i \gamma$ are displayed in Fig.2. In our paper, we adopt the general phase-space-slicing method [21] to separate the soft photon emission singularity from the real photon emission process. By using this method, the bremsstrahlung phase space is divided into singular and non-singular regions. Then the correction of the real photon emission is broken down into corresponding soft and hard terms

$$\Delta \hat{\sigma}_{real}^{EW} = \Delta \hat{\sigma}_{soft}^{EW} + \Delta \hat{\sigma}_{hard}^{EW} = \hat{\sigma}_0 (\hat{\delta}_{soft}^{EW} + \hat{\delta}_{hard}^{EW}). \quad (2.21)$$

In the c.m.s. frame, the radiated photon energy $k^0 = \sqrt{|\vec{k}|^2 + m_\gamma^2}$ is called ‘soft’ if $k^0 \leq \Delta E_\gamma$ or ‘hard’ if $k^0 > \Delta E_\gamma$. Here, m_γ is a small photon mass, which is used to regulate the infrared divergences existing in the soft term. Although both $\Delta \hat{\sigma}_{soft}^{EW}$ and $\Delta \hat{\sigma}_{hard}^{EW}$ depend on the soft photon cutoff $\Delta E_\gamma/E_b$, where $E_b = \frac{\sqrt{\hat{s}}}{2}$ is the electron beam energy in the c.m.s.

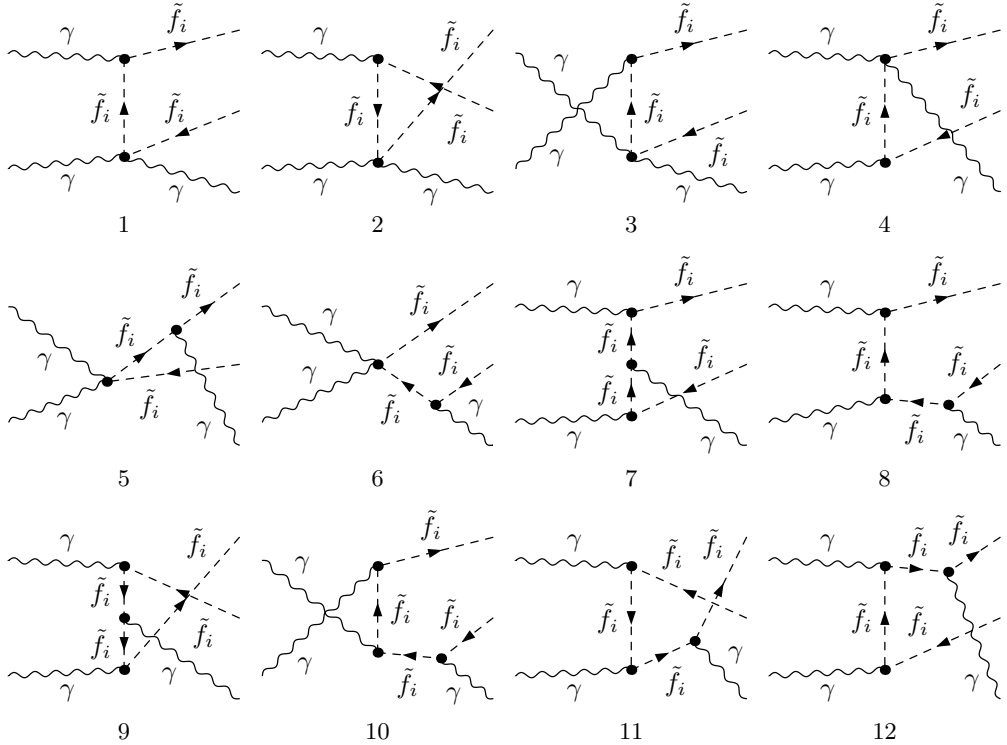


Figure 2: The real photon emission diagrams for the process $\gamma\gamma \rightarrow \tilde{f}_i \bar{\tilde{f}}_i \gamma$ ($f = \tau, t, b$)

frame, the real correction $\Delta\hat{\sigma}_{real}^{EW}$ is cutoff independent. In the calculation of soft term, we use the soft photon approximation. Since the diagrams in Fig.2 with real photon radiation from the internal sfermion line or photon-sfermions vertex do not lead to IR-singularity, we can neglect them in the calculation of soft photon emission subprocesses (2.20) by using the soft photon approximation method. In this approach the contribution of the soft photon emission subprocess is expressed as[19, 22]

$$d\Delta\hat{\sigma}_{soft}^{EW} = -d\hat{\sigma}_0 \frac{\alpha_{ew} Q_f^2}{2\pi^2} \int_{|\vec{k}| \leq \Delta E_\gamma} \frac{d^3 k}{2k^0} \left[\frac{p_3}{p_3 \cdot k} - \frac{p_4}{p_4 \cdot k} \right]^2 \quad (2.22)$$

where the soft photon cutoff ΔE_γ satisfies $k^0 \leq \Delta E_\gamma \ll \sqrt{\hat{s}}$. The integral over the soft photon phase space has been implemented in Ref.[19], then one can obtain the analytical result of the soft real photon emission correction to $\gamma\gamma \rightarrow \tilde{f}_i \bar{\tilde{f}}_i$.

As mentioned above, the IR divergence of the virtual photonic corrections can be exactly cancelled by that of soft real correction. Therefore, $\Delta\hat{\sigma}_{vir+soft}^{EW}$, the sum of the $\mathcal{O}(\alpha_{ew})$ virtual and soft contributions, is independent of the IR regulator m_γ . In the following numerical calculations, we have checked the cancellation of IR divergencies and verified that the total contributions of soft photon emission and the virtual corrections are numerically independent of m_γ . In addition, we present the numerical verification of that the total one-loop level EW correction to the cross section of $\gamma\gamma \rightarrow \tilde{f}_i \bar{\tilde{f}}_i$, defined as $\Delta\hat{\sigma}^{EW} = \Delta\hat{\sigma}_{vir}^{EW} + \Delta\hat{\sigma}_{real}^{EW}$, is independent of the cutoff ΔE_γ .

Finally, we get an UV and IR finite $\mathcal{O}(\alpha_{ew})$ EW correction $\Delta\hat{\sigma}^{EW}$:

$$\Delta\hat{\sigma}^{EW} = \Delta\hat{\sigma}_{vir}^{EW} + \Delta\hat{\sigma}_{real}^{EW} = \hat{\sigma}_0\hat{\delta}^{EW}$$

where $\hat{\delta}^{EW} = \hat{\delta}_{vir}^{EW} + \hat{\delta}_{soft}^{EW} + \hat{\delta}_{hard}^{EW}$ is the $\mathcal{O}(\alpha_{ew})$ EW relative correction.

2.3 $\mathcal{O}(\alpha_s)$ QCD correction to subprocess $\gamma\gamma \rightarrow \tilde{q}_i\bar{\tilde{q}}_i$ ($q = t, b$, $i = 1, 2$)

In this subsection, we calculate the supersymmetric $\mathcal{O}(\alpha_s)$ QCD corrections. The relevant Feynman diagrams and the corresponding amplitudes of the subprocess $\gamma\gamma \rightarrow \tilde{q}_i\bar{\tilde{q}}_i$, ($q = t, b$, $i = 1, 2$) both at tree-level and at one-loop level, are again generated by the package FeynArts 3 [20]. The Feynman diagrams of the one-loop $\mathcal{O}(\alpha_s)$ QCD corrections also can be classified into self-energy, vertex, box and counter-term diagrams. The relevant renormalized constants used in the calculation are similar with those in the calculation of the one-loop $\mathcal{O}(\alpha_{ew})$ EW correction, which are defined and expressed as in Eqs.(2.16) and Eqs.(2.18) respectively, except all the EW one-loop self-energies are replaced by the corresponding QCD ones. The SUSY QCD unrenormalized self-energy of the scalar quark \tilde{q}_i ($q = t, b, i = 1, 2$) can be written as a summation of three parts as the follows:

$$\Sigma_{ii}^{\tilde{q}}(p^2) = \Sigma_{ii}^{\tilde{q}(g)}(p^2) + \Sigma_{ii}^{\tilde{q}(\tilde{g})}(p^2) + \Sigma_{ii}^{\tilde{q}(\tilde{q})}(p^2), \quad (2.23)$$

where $\Sigma_{ii}^{\tilde{q}(g)}$, $\Sigma_{ii}^{\tilde{q}(\tilde{g})}$ and $\Sigma_{ii}^{\tilde{q}(\tilde{q})}$ denote the scalar quark self-energy parts corresponding to the diagrams with virtual gluon, virtual gluino exchanges and the squark quartic interactions respectively. The squark quartic interactions are introduced by the superpotential of the SUSY model. The three parts from the squark \tilde{q}_i self-energy can be written explicitly as

$$\Sigma_{ii}^{\tilde{q}(g)}(p^2) = -\frac{g_s^2 C_F}{16\pi^2} \{ A_0[m_g] + 4p^2(B_0 + B_1)[p^2, m_g, m_{\tilde{q}_i}] + m_g^2 B_0[p^2, m_g, m_{\tilde{q}_i}] - A_0[m_{\tilde{q}_i}] \}, \quad (2.24)$$

$$\Sigma_{ii}^{\tilde{q}(\tilde{g})}(p^2) = -\frac{g_s^2 C_F}{16\pi^2} D \{ A_0[m_g] + (m_{\tilde{g}}^2 + m_g m_{\tilde{g}} \sin 2\theta_{\tilde{q}}) B_0[p^2, m_{\tilde{g}}, m_g] + p^2 B_1[p^2, m_{\tilde{g}}, m_g] \}, \quad (2.25)$$

$$\Sigma_{ii}^{\tilde{q}(\tilde{q})}(p^2) = \frac{g_s^2}{12\pi^2} \{ A_0[m_{\tilde{q}_1}^2] \cos^2 2\theta_{\tilde{q}} + A_0[m_{\tilde{q}_2}^2] \sin^2 2\theta_{\tilde{q}} \}, \quad (2.26)$$

where m_g denotes the small gluon mass, $D = 4 - 2\epsilon$ is the space-time dimension and the group Casimir operator has $C_F = \frac{4}{3}$.

The one-loop $\mathcal{O}(\alpha_s)$ QCD virtual correction of subprocess $\gamma\gamma \rightarrow \tilde{q}_i\bar{\tilde{q}}_i$ ($q = t, b$, $i = 1, 2$) can be expressed as

$$\Delta\hat{\sigma}_{vir}^{QCD} = \hat{\sigma}_0\hat{\delta}_{vir}^{QCD} = \frac{1}{16\pi^2 \hat{s}^2} \int_{\hat{t}_{min}}^{\hat{t}_{max}} d\hat{t} \, 2Re \sum (M_{vir}^{QCD} M_0^\dagger) \quad (2.27)$$

where M_{vir}^{QCD} is the renormalized amplitude of the one-loop $\mathcal{O}(\alpha_s)$ QCD Feynman diagrams, which include self-energy, vertex, box and counter-term diagrams.

The virtual QCD corrections contain both ultraviolet (UV) and infrared (IR) divergences in general. To regularize the UV divergences in loop integrals, we adopt the dimensional regularization in which the dimensions of spinor and space-time manifolds are extended to $D = 4 - 2\epsilon$. We have verified the cancellation of the UV divergence both

analytically and numerically. Then we get a UV finite amplitude including $\mathcal{O}(\alpha_s)$ virtual radiative corrections. The IR divergence of the QCD virtual corrections of the subprocess $\gamma\gamma \rightarrow \tilde{q}_i \bar{\tilde{q}}_i$ ($q = t, b$, $i = 1, 2$) coming from virtual gluonic correction can be cancelled by the real soft gluonic bremsstrahlung, which is analogous to the real soft photonic one. The real gluon emission diagrams of the process $\gamma + \gamma \rightarrow \tilde{q}_i \bar{\tilde{q}}_i g$ are shown in Fig.3. We denote the real gluon emission as

$$\gamma(p_1) + \gamma(p_2) \rightarrow \tilde{q}_i(p_3) + \bar{\tilde{q}}_i(p_4) + g(k), \quad (q = t, b, \quad i = 1, 2). \quad (2.28)$$

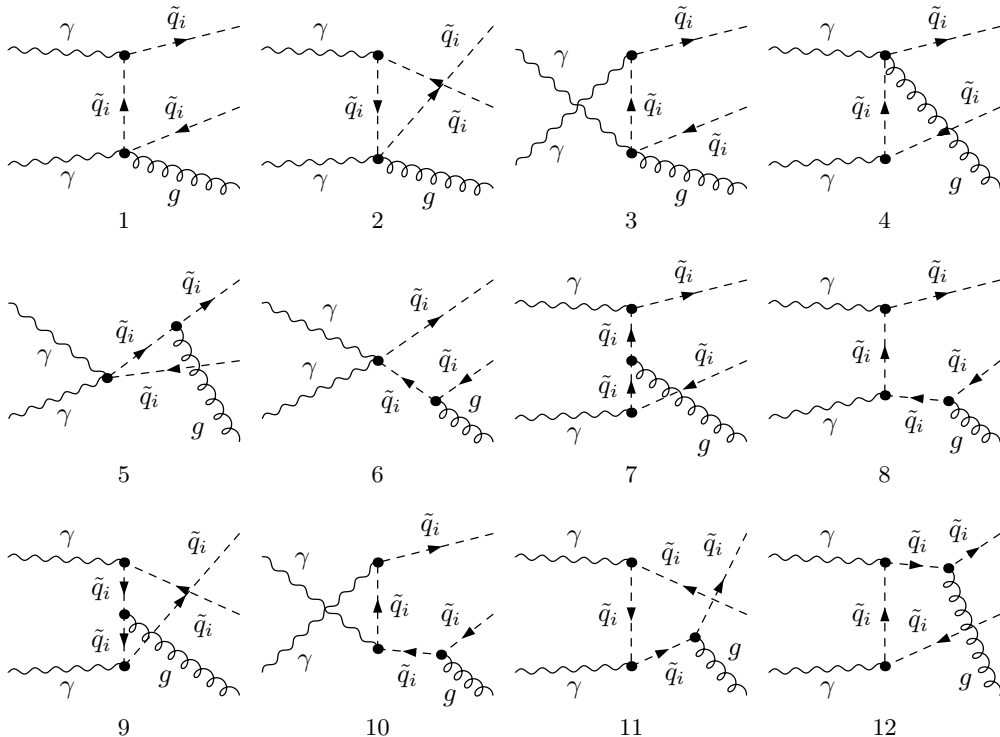


Figure 3: The real gluon emission diagrams for the process $\gamma\gamma \rightarrow \tilde{q}_i \bar{\tilde{q}}_i g$ ($q = t, b$, $i = 1, 2$)

Analogously, we use again the general phase-space-slicing method to separate the soft gluon emission singularity from the real gluon emission process. Therefore, the correction of the real gluon emission is divided into soft and hard terms

$$\Delta\hat{\sigma}_{real}^{QCD} = \Delta\hat{\sigma}_{soft}^{QCD} + \Delta\hat{\sigma}_{hard}^{QCD} = \hat{\sigma}_0(\hat{\delta}_{soft}^{QCD} + \hat{\delta}_{hard}^{QCD}) \quad (2.29)$$

By using the soft gluon approximation, we get the contribution of the soft gluon emission subprocess expressed as

$$d\Delta\hat{\sigma}_{soft}^{QCD} = -d\hat{\sigma}_0 \frac{\alpha_s C_F}{2\pi^2} \int_{|\vec{k}| \leq \Delta E_g} \frac{d^3 k}{2k^0} \left[\frac{p_3}{p_3 \cdot k} - \frac{p_4}{p_4 \cdot k} \right]^2 \quad (2.30)$$

in which ΔE_g is the energy cutoff of the soft gluon and $k^0 \leq \Delta E_g \ll \sqrt{\hat{s}}$. $k^0 = \sqrt{|\vec{k}|^2 + m_g^2}$ is the gluon energy. p_3 and p_4 are the four momenta of two final state particles \tilde{q}_i and $\bar{\tilde{q}}_i$.

In this approach, we may again refer to Ref.[19] to get the analytical expression of the soft gluon correction.

Finally we obtain an UV and IR finite $\mathcal{O}(\alpha_s)$ QCD correction $\Delta\hat{\sigma}^{QCD}$ to the subprocess $\gamma\gamma \rightarrow \tilde{q}_i\bar{\tilde{q}}_i$ containing one-loop $\mathcal{O}(\alpha_s)$ QCD correction

$$\Delta\hat{\sigma}^{QCD} = \Delta\hat{\sigma}_{vir}^{QCD} + \Delta\hat{\sigma}_{real}^{QCD} = \hat{\sigma}_0 \hat{\delta}^{QCD} \quad (2.31)$$

where $\hat{\delta}^{QCD} = \hat{\delta}_{vir}^{QCD} + \hat{\delta}_{soft}^{QCD} + \hat{\delta}_{hard}^{QCD}$ is the $\mathcal{O}(\alpha_s)$ QCD relative correction.

2.4 The cross sections of parent processes $e^+e^- \rightarrow \gamma\gamma \rightarrow \tilde{f}_i\bar{\tilde{f}}_i$ ($f = \tau, t, b$, $i = 1, 2$)

The $\tilde{f}_i\bar{\tilde{f}}_i$ pair production via photon-photon fusion is only a subprocess of the parent process $e^+e^- \rightarrow \gamma\gamma \rightarrow \tilde{f}_i\bar{\tilde{f}}_i$. The laser back-scattering technique on electron beam can transform e^+e^- beams into photon beams [23, 24, 25]. After integrating over the photon luminosity in an e^+e^- linear collider, we obtain the total cross section of the process $e^+e^- \rightarrow \gamma\gamma \rightarrow \tilde{f}_i\bar{\tilde{f}}_i$ expressed

$$\sigma(s) = \int_{2m_{\tilde{f}_i}/\sqrt{s}}^{x_{max}} dz \frac{dL_{\gamma\gamma}}{dz} \hat{\sigma}(\gamma\gamma \rightarrow \tilde{f}_i\bar{\tilde{f}}_i \text{ at } \hat{s} = z^2 s), \quad (2.32)$$

where \sqrt{s} and $\sqrt{\hat{s}}$ are the e^+e^- and $\gamma\gamma$ c.m.s. energies respectively and $dL_{\gamma\gamma}/dz$ is the distribution function of photon luminosity, which is expressed as

$$\frac{dL_{\gamma\gamma}}{dz} = 2z \int_{z^2/x_{max}}^{x_{max}} \frac{dx}{x} f_{\gamma/e}(x) f_{\gamma/e}(z^2/x) \quad (2.33)$$

where $f_{\gamma/e}$ is the photon structure function of the electron beam [18, 27]. For the initial unpolarized electrons and laser photon beams, the photon structure function is given by the most promising Compton backscattering as [18, 28, 29]

$$f_{\gamma/e} = \frac{1}{D(\xi)} \left[1 - x + \frac{1}{1-x} - \frac{4x}{\xi(1-x)} + \frac{4x^2}{\xi^2(1-x)^2} \right], \quad (2.34)$$

where

$$D(\xi) = \left(1 - \frac{4}{\xi} - \frac{8}{\xi^2} \right) \ln(1+\xi) + \frac{1}{2} + \frac{8}{\xi} - \frac{1}{2(1+\xi)^2},$$

$$\xi = \frac{2\sqrt{s}\omega_0}{m_e^2}. \quad (2.35)$$

m_e and $\sqrt{s}/2$ represent the mass and energy of the electron respectively. ω_0 is the laser-photon energy and x is the fraction of the energy of the incident electron carried by the backscattered photon. The maximum fraction of energy carried by the backscattered photon is $x_{max} = 2\omega_{max}/\sqrt{s} = \xi/(1+\xi)$. In our calculations, we choose ω_0 to maximize the backscattered photon energy without spoiling the luminosity through e^+e^- pair creation. Then we have $\xi = 2(1 + \sqrt{2})$, $x_{max} \simeq 0.83$, and $D(\xi) \approx 1.8397$ [26].

3 Numerical results

In this section, we present some numerical results for the one loop $\mathcal{O}(\alpha_s)$ QCD and $\mathcal{O}(\alpha_{ew})$ EW corrections to subprocesses $\gamma\gamma \rightarrow \tilde{f}_i \tilde{f}_i$ and the parent processes $e^+e^- \rightarrow \gamma\gamma \rightarrow \tilde{f}_i \tilde{f}_i$. In our numerical calculation, the SM parameters are set to be $\alpha_s(m_Z^2) = 0.1190$, $m_e = 0.5110998902$ MeV, $m_\mu = 105.658357$ MeV, $m_\tau = 1.77699$ GeV, $m_u = 66$ MeV, $m_d = 66$ MeV, $m_c = 1.2$ GeV, $m_s = 150$ MeV, $m_b = 4.3$ GeV, $m_t = 174.3$ GeV, $m_Z = 91.1876$ GeV, $m_W = 80.423$ GeV[31]. There we use the effective values of the light quark masses (m_u and m_d) which can reproduce the hadron contribution to the shift in the fine structure constant $\alpha_{ew}(m_Z^2)$ [32]. We take the fine structure constant at the Z^0 -pole as input parameter, $\alpha_{ew}(m_Z^2)^{-1}|_{\overline{MS}} = 127.918$ [31]. Then from Eq.(2.17) we get the counter-term of the electric charge in \overline{DR} scheme expressed as [33, 34, 13]

$$\begin{aligned} \delta Z_e = & \frac{e^2}{6(4\pi)^2} \left\{ 4 \sum_f N_C^f e_f^2 \left(\Delta + \log \frac{Q^2}{x_f^2} \right) + \sum_{\tilde{f}} \sum_{k=1}^2 N_C^f e_f^2 \left(\Delta + \log \frac{Q^2}{m_{\tilde{f}_k}^2} \right) \right. \\ & + 4 \sum_{k=1}^2 \left(\Delta + \log \frac{Q^2}{m_{\tilde{\chi}_k}^2} \right) + \sum_{k=1}^2 \left(\Delta + \log \frac{Q^2}{m_{H_k^+}^2} \right) \\ & \left. - 22 \left(\Delta + \log \frac{Q^2}{m_W^2} \right) \right\}, \end{aligned} \quad (3.1)$$

where we take $x_f = m_Z$ when $m_f < m_Z$ and $x_t = m_t$. Q_f is the electric charge of (s)fermion and $\Delta = 2/\epsilon - \gamma + \log 4\pi$. N_C^f is color factor, which equal to 1 and 3 for (s)leptons and (s)quarks, respectively. It is obvious that there is a little discrepancy between our electric charge counter-term expression(Eq.(3.1)) and that in subsection 3.1 of Ref.[13].

The MSSM parameters are determined by using FormCalc package with following input parameters[35]:

(1) The input parameters for MSSM Higgs sector are the CP-odd mass M_{A^0} and $\tan\beta$ with the constraint $\tan\beta \geq 2.5$. The masses of the MSSM Higgs sector are fixed by taking into account the significant radiative corrections.

(2) The input parameters for the chargino and neutralino sector are the gaugino mass parameters M_1 , M_2 and the Higgsino-mass parameter μ . We adopt the grand unification theory(GUT) relation $M_1 = (5/3) \tan^2 \theta_W M_2$ for simplification [30] and the gluino mass $m_{\tilde{g}}$ is evaluated by $m_{\tilde{g}} = \alpha_s(Q)/\alpha_{ew}(m_Z) \sin^2 \theta_W M_2$.

(3) For the sfermion sector, we assume $M_{\tilde{Q}} = M_{\tilde{U}} = M_{\tilde{D}} = M_{\tilde{E}} = M_{\tilde{L}} = M_{SUSY}$ and take the soft trilinear couplings for sfermions \tilde{q} and \tilde{l} being equal, i.e., $A_q = A_l = A_f$.

Except above SM and MSSM input parameters, we should have some other parameters used in our numerical calculations, for example, the QCD renormalization scale Q , the IR regularization parameter $m_\gamma(m_g)$ and the soft cutoff $\Delta E_{\gamma,g}/E_b$. In our following numerical calculations, we take the QCD renormalization scale Q to be $2m_{\tilde{f}_i}$, and set $\Delta E_{\gamma,g}/E_b = 10^{-3}$, $m_{\gamma,g} = 10^{-5}$ GeV, if there is no other statement. As we know, the final results should be independent on IR regulator $m_{\gamma,g}$ and the cutoff $\Delta E_{\gamma,g}/E_b$. For demonstration, we present the dependence of the $\mathcal{O}(\alpha_s)$ QCD corrections to $\gamma\gamma \rightarrow \tilde{t}_1 \tilde{t}_1$ ($m_{\tilde{t}_1} = 148$ GeV) in conditions of $\sqrt{s} = 500$ GeV and *Set1* parameters(see below) on the soft cutoff $\Delta E_g/E_b$ in Fig.4. The full,

dashed and dotted lines correspond to $\Delta\hat{\sigma}_{vir+soft}^{QCD}$, $\Delta\hat{\sigma}_{hard}^{QCD}$ and the total correction $\Delta\hat{\sigma}^{QCD}$. As shown in this figure, the full $\mathcal{O}(\alpha_s)$ one-loop QCD correction $\Delta\hat{\sigma}^{QCD}$ is independent of the soft cutoff $\Delta E_g/E_b$ as $\Delta E_g/E_b$ running from 10^{-5} to 10^{-2} , although both $\Delta\hat{\sigma}_{vir+soft}^{QCD}$ and $\Delta\hat{\sigma}_{hard}^{QCD}$ depend on cutoff strongly.

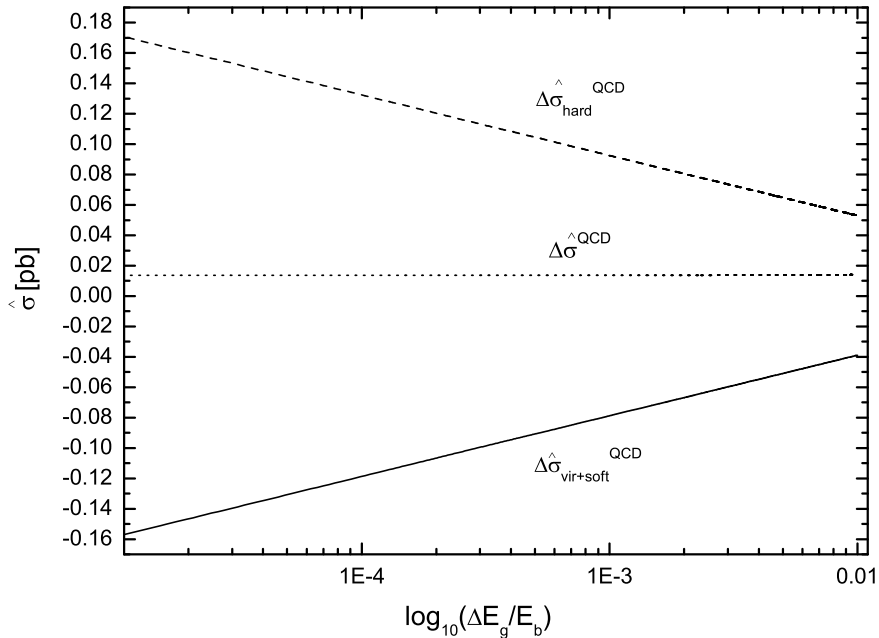


Figure 4: The full $\mathcal{O}(\alpha_s)$ QCD corrections to $\gamma\gamma \rightarrow \tilde{t}_1\bar{\tilde{t}}_1$ as a function of the soft gluon cutoff $\Delta E_g/E_b$ in conditions of $\sqrt{\hat{s}} = 500$ GeV and *Set1* parameters.

In order to show and discuss the effects of the radiative corrections to the subprocess of $\gamma\gamma \rightarrow \tilde{f}_i\bar{\tilde{f}}_i$ quantitatively, we choose the following four typical data sets:

Set1: $\tan\beta = 6$, $M_{A^0} = 250$ GeV, $M_{SUSY} = 200$ GeV, $\mu = 800$ GeV, $M_2 = 200$ GeV and $A_f = 400$ GeV.

Then we have $m_{\tilde{\tau}_{1,2}} = (185, 223)$ GeV, $m_{\tilde{t}_{1,2}} = (148, 340)$ GeV and $m_{\tilde{b}_{1,2}} = (146, 250)$ GeV.

Set2: $\tan\beta = 20$, $M_{A^0} = 300$ GeV, $M_{SUSY} = 400$ GeV, $\mu = 1000$ GeV, $M_2 = 200$ GeV and $A_f = -500$ GeV.

Then we have $m_{\tilde{\tau}_{1,2}} = (354, 446)$ GeV, $m_{\tilde{t}_{1,2}} = (304, 533)$ GeV and $m_{\tilde{b}_{1,2}} = (256, 508)$ GeV.

Set3: $\tan\beta = 30$, $M_{A^0} = 300$ GeV, $M_{SUSY} = 250$ GeV, $\mu = -200$ GeV, $M_2 = 800$ GeV and $A_f = 250$ GeV.

Then we have $m_{\tilde{\tau}_{1,2}} = (231, 275)$ GeV, $m_{\tilde{t}_{1,2}} = (215, 368)$ GeV and $m_{\tilde{b}_{1,2}} = (188, 307)$ GeV.

Set4: $\tan \beta = 30$, $M_{A^0} = 250$ GeV, $M_{SUSY} = 200$ GeV, $\mu = 200$ GeV, $M_2 = 1000$ GeV and $A_f = 300$ GeV.

Then we have $m_{\tilde{\tau}_{1,2}} = (179, 228)$ GeV, $m_{\tilde{t}_{1,2}} = (131, 346)$ GeV and $m_{\tilde{b}_{1,2}} = (124, 263)$ GeV.

With the input parameters $\tan \beta$, M_{A^0} , M_{SUSY} , μ , M_2 and A_f in above data sets, all the masses of supersymmetric particles can be obtained by using package FormCalc. *Set1*(or *Set2*) is the case of gaugino-like with small(or mediate) $\tan \beta$, but lighter(or heavier) sfermions, while *Set3* and *Set4* are higgsino-like case with larger $\tan \beta$.

The Born and the full $\mathcal{O}(\alpha_{ew})$ EW corrected cross sections for the $\gamma\gamma \rightarrow \tilde{\tau}_1 \bar{\tilde{\tau}}_1$ subprocess as the functions of c.m.s. energy of $\gamma\gamma$ collider with above four data sets are displayed in Fig.5(a). There $\hat{\sigma}_{0,i}$'s are the Born cross sections and $\hat{\sigma}_{1,i}$'s are the full $\mathcal{O}(\alpha_{ew})$ EW corrected cross sections for the subprocess $\gamma\gamma \rightarrow \tilde{\tau}_1 \bar{\tilde{\tau}}_1$. The subscript i goes from 1 to 4, which correspond to the data *Set1*, *Set2*, *Set3* and *Set4* respectively. The $\mathcal{O}(\alpha_{ew})$ EW corrected cross section with *Set4* can achieve the maximal value 0.278 pb at the energy near the threshold $\sqrt{\hat{s}} \sim 400$ GeV. When $\sqrt{\hat{s}}$ approaches to 1.5 TeV, the EW corrected cross section with *Set2* goes down to 27.5 fb, but it is still much larger than that for the process of $e^+e^- \rightarrow \tilde{\tau}_1 \bar{\tilde{\tau}}_1$ [13, 14] with the same input parameters. In Fig.5(b), the relative $\mathcal{O}(\alpha_{ew})$ EW corrections with the four data sets are depicted. As it can be seen in this figure, the relative corrections $\hat{\delta}$ also have their maximal values at the position near the threshold energies and then decrease quantitatively with the increment of $\sqrt{\hat{s}}$. When the c.m.s. energy $\sqrt{\hat{s}}$ goes from the threshold value of $\tilde{\tau}_1 \bar{\tilde{\tau}}_1$ pair production to 2 TeV, the full $\mathcal{O}(\alpha_{ew})$ EW corrections can enhance or reduce the Born cross section depending on the colliding energy. At the position of colliding energy $\sqrt{\hat{s}} = 2$ TeV, the relative EW correction $\hat{\delta}$ can reach -24.6% , -24.1% , -23.5% and -23.2% for *Set1*, *Set2*, *Set3* and *Set4* respectively. Fig.5(c) shows the numerical results of the cross sections of $\gamma\gamma \rightarrow \tilde{\tau}_2 \bar{\tilde{\tau}}_2$ subprocess both at the Born level and one-loop level, as the functions of the colliding energy $\sqrt{\hat{s}}$. Fig.5(d) displays the relative $\mathcal{O}(\alpha_{ew})$ EW correction for $\tilde{\tau}_2 \bar{\tilde{\tau}}_2$ -pair production as a function of $\sqrt{\hat{s}}$. We find that the behavior of curves in Fig.5(c), which correspond to the Born, the EW corrected cross sections of $\tilde{\tau}_2 \bar{\tilde{\tau}}_2$ production, are quite similar to those in Fig.5(a) for $\tilde{\tau}_1 \bar{\tilde{\tau}}_1$ production. But the values of the cross sections for $\tilde{\tau}_2 \bar{\tilde{\tau}}_2$ production are always smaller due to the heavier mass of $\tilde{\tau}_2$, and can reach 0.173 pb near the threshold energy of $\tilde{\tau}_2 \bar{\tilde{\tau}}_2$ pair production in the case of *Set1*. The magnitude of EW relative correction is about -26.1% or -24.5% at the position of $\sqrt{\hat{s}} = 2$ TeV, which is close to that of $\gamma\gamma \rightarrow \tilde{\tau}_1 \bar{\tilde{\tau}}_1$ subprocess.

In Fig.6(a) and Fig.6(c), we depict the full $\mathcal{O}(\alpha_{ew})$ EW and $\mathcal{O}(\alpha_s)$ QCD corrected cross sections for the subprocess $\gamma\gamma \rightarrow \tilde{t}_1 \bar{\tilde{t}}_1$. Analogously, $\hat{\sigma}_{0,i}$ ($i = 1 \dots, 4$) mean the tree-level cross sections corresponding to the four input data sets respectively, and $\hat{\sigma}_{1,i}$'s are the full one-loop corrected cross sections. Fig.6(a) demonstrates that the corresponding two curves for Born and $\mathcal{O}(\alpha_{ew})$ EW corrected cross sections in the same condition of the input data set, have the same line shape. While Fig.6(c) shows obviously that the $\mathcal{O}(\alpha_s)$ QCD corrections can be larger than the $\mathcal{O}(\alpha_{ew})$ EW corrections, especially near the threshold. The EW and QCD relative corrections to $\tilde{t}_1 \bar{\tilde{t}}_1$ pair production subprocess are displayed in Fig.6(b) and (d), respectively. From Fig.6(b), we can see that the $\mathcal{O}(\alpha_{ew})$ EW relative corrections to $\gamma\gamma \rightarrow \tilde{t}_1 \bar{\tilde{t}}_1$ subprocess vary from positive values to negative ones as $\sqrt{\hat{s}}$ running from the threshold value to 2 TeV. The absolute value of the relative correction $|\hat{\delta}^{EW}|$ for *Set3* can reach about 34.2%

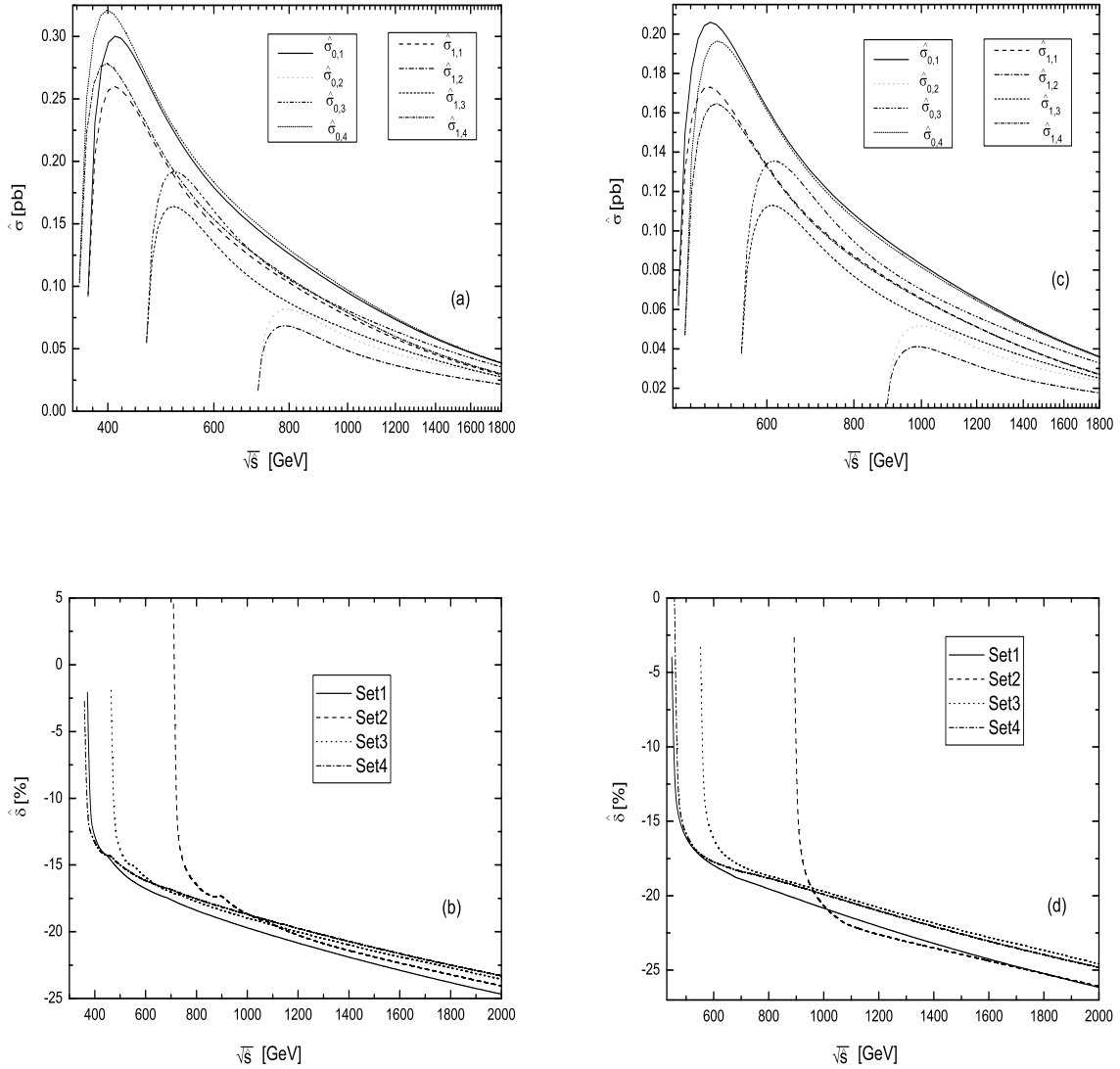


Figure 5: (a) The Born and full $\mathcal{O}(\alpha_{ew})$ EW corrected cross sections for the $\gamma\gamma \rightarrow \tilde{\tau}_1 \bar{\tilde{\tau}}_1$ subprocess as the functions of c.m.s. energy of $\gamma\gamma$ collider \sqrt{s} with four different data sets, respectively. (b) The full $\mathcal{O}(\alpha_{ew})$ EW relative correction to the $\gamma\gamma \rightarrow \tilde{\tau}_1 \bar{\tilde{\tau}}_1$ subprocess. The solid, dashed, dotted and dash-dotted curves correspond to four different data set cases, respectively. (c) The Born and full $\mathcal{O}(\alpha_{ew})$ EW corrected cross sections for the $\gamma\gamma \rightarrow \tilde{\tau}_2 \bar{\tilde{\tau}}_2$ subprocess as the functions of c.m.s. energy of $\gamma\gamma$ collider \sqrt{s} with four different data sets, respectively. (d) The full $\mathcal{O}(\alpha_{ew})$ EW relative correction to the $\gamma\gamma \rightarrow \tilde{\tau}_2 \bar{\tilde{\tau}}_2$ subprocess. The solid, dashed, dotted and dash-dotted curves correspond to four different data set cases, respectively.

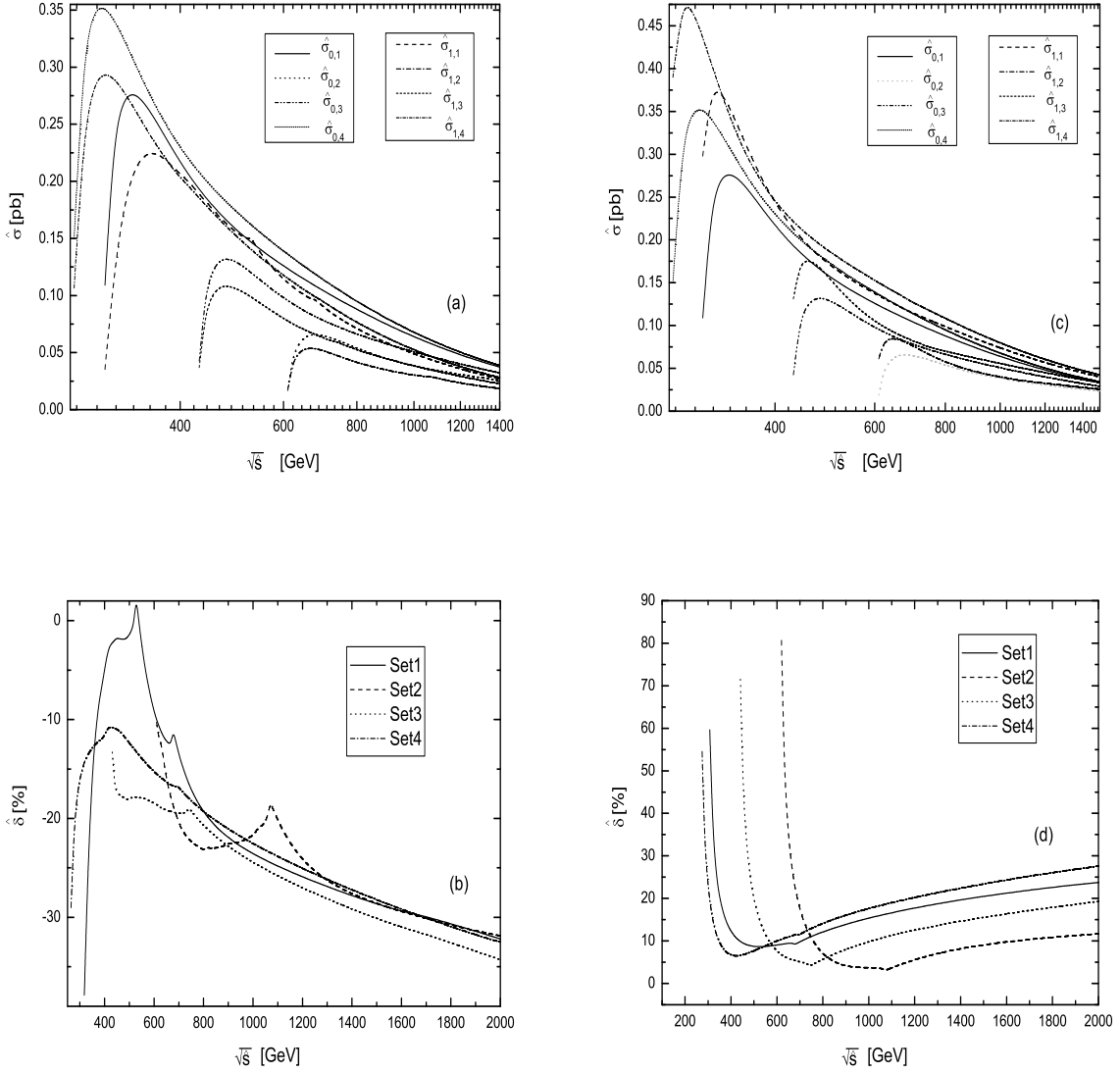


Figure 6: (a) The Born and full $\mathcal{O}(\alpha_{ew})$ EW corrected cross sections for the $\gamma\gamma \rightarrow \tilde{t}_1 \tilde{t}_1$ subprocess as the functions of c.m.s. energy of $\gamma\gamma$ collider $\sqrt{\hat{s}}$ with four different data sets, respectively. (b) The full $\mathcal{O}(\alpha_{ew})$ EW relative correction to $\gamma\gamma \rightarrow \tilde{t}_1 \tilde{t}_1$ subprocess. Four different curves correspond to four different data sets, respectively. (c) The Born and full $\mathcal{O}(\alpha_s)$ QCD corrected cross sections for the $\gamma\gamma \rightarrow \tilde{t}_1 \tilde{t}_1$ subprocess as the functions of c.m.s. energy of $\gamma\gamma$ collider $\sqrt{\hat{s}}$ with four different data sets, respectively. (d) The full $\mathcal{O}(\alpha_s)$ QCD relative correction to $\gamma\gamma \rightarrow \tilde{t}_1 \tilde{t}_1$ subprocess.

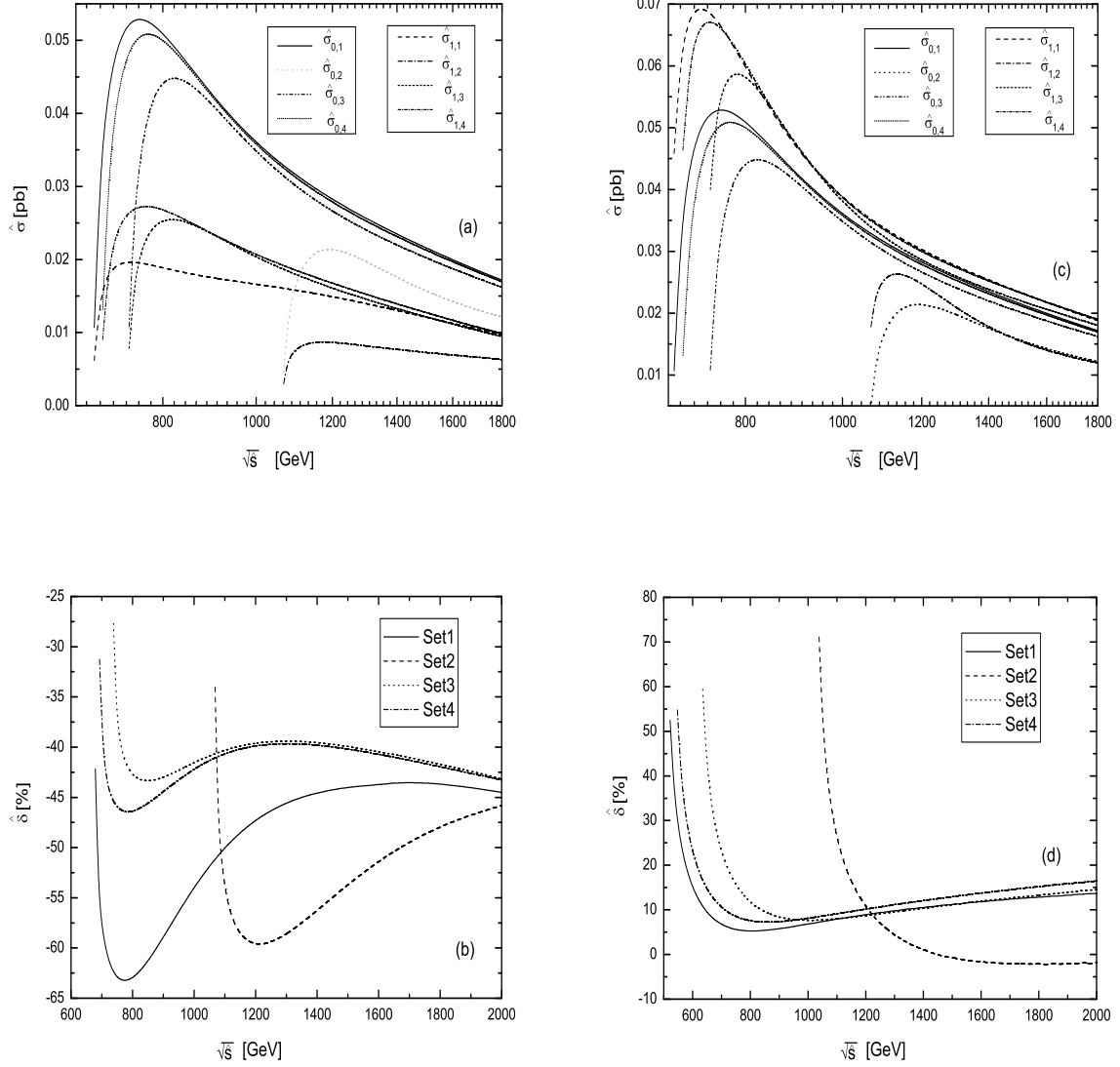


Figure 7: (a) The Born and full $\mathcal{O}(\alpha_{ew})$ EW corrected cross sections for the $\gamma\gamma \rightarrow \tilde{t}_2\tilde{t}_2$ subprocess as the functions of c.m.s. energy of $\gamma\gamma$ collider \sqrt{s} with four different data sets, respectively. (b) The full $\mathcal{O}(\alpha_{ew})$ EW relative correction to $\gamma\gamma \rightarrow \tilde{t}_2\tilde{t}_2$ subprocess. Four different curves correspond to four different data sets, respectively. (c) The Born and full $\mathcal{O}(\alpha_s)$ QCD corrected cross sections for the $\gamma\gamma \rightarrow \tilde{t}_2\tilde{t}_2$ subprocess as the functions of c.m.s. energy of $\gamma\gamma$ collider \sqrt{s} with four different data sets, respectively. (d) The full $\mathcal{O}(\alpha_s)$ QCD relative correction to $\gamma\gamma \rightarrow \tilde{t}_2\tilde{t}_2$ subprocess.

at the point of $\sqrt{\hat{s}} = 2$ TeV and be over 32% near the threshold for *Set1*. Furthermore, with the same input parameters as used in [13], for example, *Set2*, our calculation shows that, when $\sqrt{\hat{s}}$ is between 1200 GeV and 2000 GeV, the EW relative correction to $\gamma\gamma \rightarrow \tilde{t}_1\bar{\tilde{t}}_1$ subprocess is about $-24.1 \sim -31.8\%$, while the EW relative correction to $e^+e^- \rightarrow \tilde{t}_1\bar{\tilde{t}}_1$ process is about -10% [13]. We notice that on the curves in Fig.6(b) there are some small spikes which are due to the resonance effects. For example, the resonance effect at the position of $\sqrt{\hat{s}} \sim 525$ GeV is caused by $\sqrt{\hat{s}} \sim 2m_{H^+}$ for input data *Set1*, while the resonance effect at the position of $\sqrt{\hat{s}} \sim 1066$ GeV is caused by $\sqrt{\hat{s}} \sim 2m_{\tilde{t}_2}$ for input data *Set2*. Furthermore, when we observe Fig.6(d), which shows the relative QCD correction as a function of c.m.s. energy $\sqrt{\hat{s}}$ for $\gamma\gamma \rightarrow \tilde{t}_1\bar{\tilde{t}}_1$, we can see that the values of $\hat{\delta}^{QCD}$ decrease rapidly to minimal values after $\sqrt{\hat{s}}$ just goes up from the threshold energy and then increase slowly to 23.8%, 11.4%, 19.3% and 27.6% at the position of $\sqrt{\hat{s}} = 2$ TeV for *Set1*, *Set2*, *Set3* and *Set4*, respectively.

The results for subprocess $\gamma\gamma \rightarrow \tilde{t}_2\bar{\tilde{t}}_2$ are drawn in Fig.7(a-d). The full $\mathcal{O}(\alpha_{ew})$ EW and $\mathcal{O}(\alpha_s)$ QCD corrected cross sections are plotted in Fig.7(a) and Fig.7(c), respectively. Comparing these two figures with Fig.6(a) and Fig.6(c), we can see that the cross sections for the $\gamma\gamma \rightarrow \tilde{t}_2\bar{\tilde{t}}_2$ subprocess are almost one order smaller than those for the $\gamma\gamma \rightarrow \tilde{t}_1\bar{\tilde{t}}_1$ subprocess quantitatively due to $m_{\tilde{t}_2} > m_{\tilde{t}_1}$. The EW and QCD relative corrections to subprocess $\gamma\gamma \rightarrow \tilde{t}_2\bar{\tilde{t}}_2$ are plotted in Fig.7(b) and Fig.7(d), respectively. From Fig.7(d), we see that the values of QCD relative corrections are rather large near the threshold, and at position of $\sqrt{\hat{s}} = 2$ TeV they are 10.2%, -0.7% , 12.5% and 13.2% for data *Set1*, *Set2*, *Set3* and *Set4* respectively, which are less than the corresponding QCD relative corrections to the $\gamma\gamma \rightarrow \tilde{t}_1\bar{\tilde{t}}_1$ subprocess shown in Fig.6(d). The absolute EW relative corrections are generally larger than those of the absolute QCD relative corrections shown in Fig.7(d), except in the threshold energy regions. The values of EW relative corrections are about -45% for the two gaugino-like data sets *Set1* and *Set2* and -43% for the two higgsino-like data sets *Set3* and *Set4* at the position of $\sqrt{\hat{s}} = 2$ TeV. The EW relative corrections to $\gamma\gamma \rightarrow \tilde{t}_2\bar{\tilde{t}}_2$ cross section are negative in the range of $\sqrt{\hat{s}} = 700 \sim 2000$ GeV with all the four data sets and have the minimal values near the position of $\sqrt{\hat{s}} = 800$ GeV for *Set1*, *Set3* and *Set4*, and in the vicinity of $\sqrt{\hat{s}} \sim 1200$ GeV for *Set2*.

We also show the $\tilde{b}_i\bar{\tilde{b}}_i$, ($i = 1, 2$) pair productions in Fig.8 and Fig.9. Fig.8(a) is plotted for the Born and full $\mathcal{O}(\alpha_{ew})$ EW corrected cross sections of the $\gamma\gamma \rightarrow \tilde{b}_1\bar{\tilde{b}}_1$ subprocess as the functions of $\sqrt{\hat{s}}$ with four data sets respectively, and Fig.8(c) for the Born and full $\mathcal{O}(\alpha_s)$ QCD corrected cross sections. Fig.8(b) and Fig.8(d) display the EW and QCD relative corrections, respectively. These figures show that the behaviors of the curves for $\tilde{b}_1\bar{\tilde{b}}_1$ pair production are similar to those for $\tilde{t}_1\bar{\tilde{t}}_1$ pair production. Comparing Fig.6(b) with Fig.8(b), we notice that the full $\mathcal{O}(\alpha_{ew})$ EW relative correction to $\gamma\gamma \rightarrow \tilde{b}_1\bar{\tilde{b}}_1$ subprocess is larger than that to the $\gamma\gamma \rightarrow \tilde{t}_1\bar{\tilde{t}}_1$ subprocess. The maximum absolute value of the former can reach 50.7% for *Set2* at the position of $\sqrt{\hat{s}} \sim 2000$ GeV, which is even larger than the QCD correction to $\gamma\gamma \rightarrow \tilde{b}_1\bar{\tilde{b}}_1$. Again, all of the small spikes appearing on the curves of Fig.8(a-b) are due to the resonance effects, such as the spikes at the positions of $\sqrt{\hat{s}} \sim 525$ GeV for *Set1* and $\sqrt{\hat{s}} \sim 621$ GeV for *Set2* are caused by $\sqrt{\hat{s}} \sim 2m_{H^+}$, while condition of $\sqrt{\hat{s}} \sim 2m_{\tilde{t}_2}$ leads to the spike at the position of $\sqrt{\hat{s}} \sim 1066$ GeV for *Set2*. In Fig.8(d), the solid, dashed, dotted and dash-dotted lines correspond to the QCD relative corrections with parameter scenarios *Set1*, *Set2*, *Set3* and *Set4*, respectively. Although Fig.8(d) demonstrates that the the QCD relative

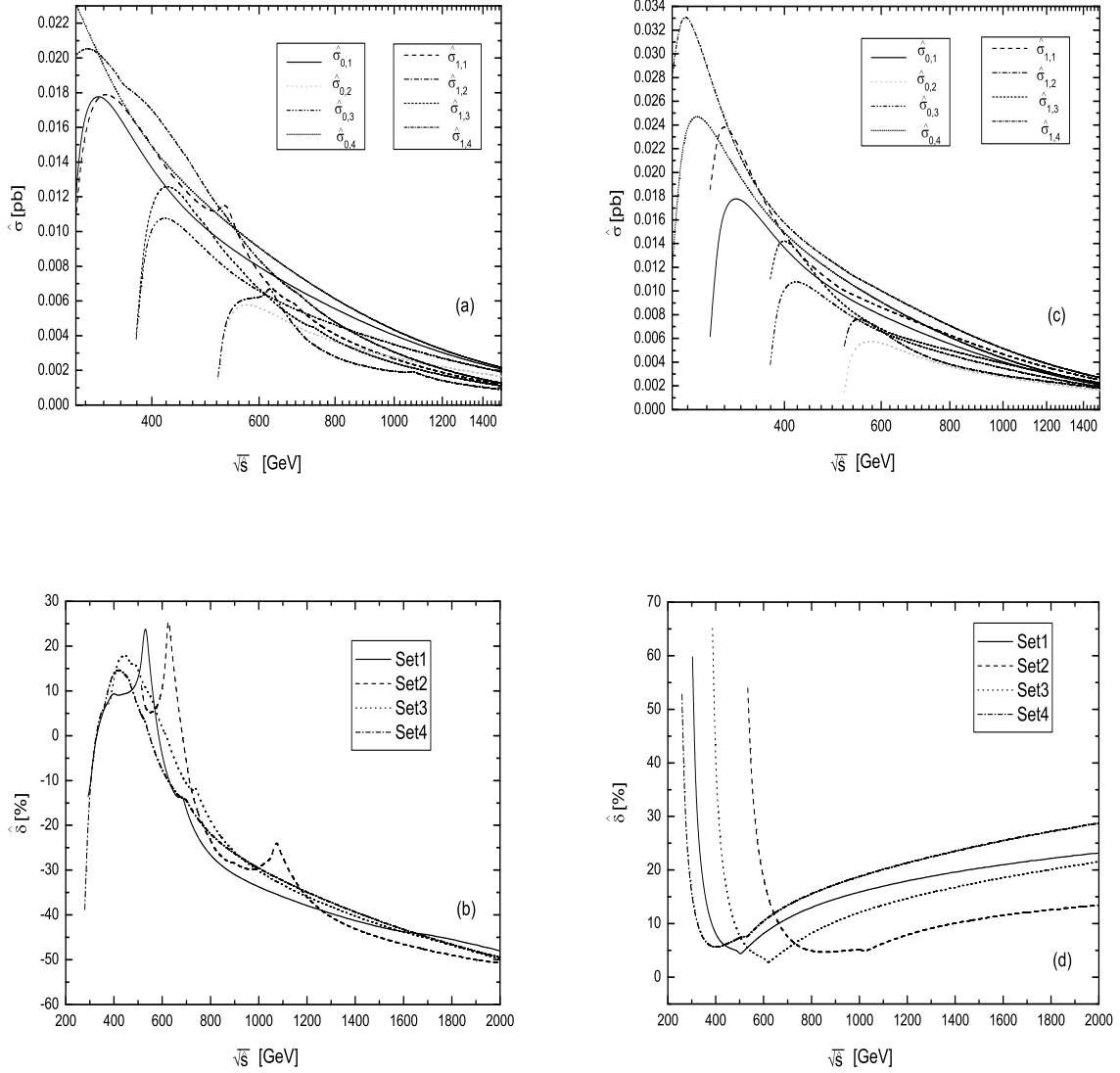


Figure 8: (a) The Born and full $\mathcal{O}(\alpha_{ew})$ EW corrected cross sections for the $\gamma\gamma \rightarrow \tilde{b}_1\bar{\tilde{b}}_1$ subprocess as the functions of c.m.s. energy \sqrt{s} with four data sets, respectively. (b) The full one-loop $\mathcal{O}(\alpha_{ew})$ EW relative correction to $\gamma\gamma \rightarrow \tilde{b}_1\bar{\tilde{b}}_1$ subprocess. (c) The Born and full $\mathcal{O}(\alpha_s)$ QCD corrected cross sections for the $\gamma\gamma \rightarrow \tilde{b}_1\bar{\tilde{b}}_1$ subprocess as the functions of c.m.s. energy \sqrt{s} with four data sets, respectively. (d) The full $\mathcal{O}(\alpha_s)$ QCD relative correction to $\gamma\gamma \rightarrow \tilde{b}_1\bar{\tilde{b}}_1$ subprocess.

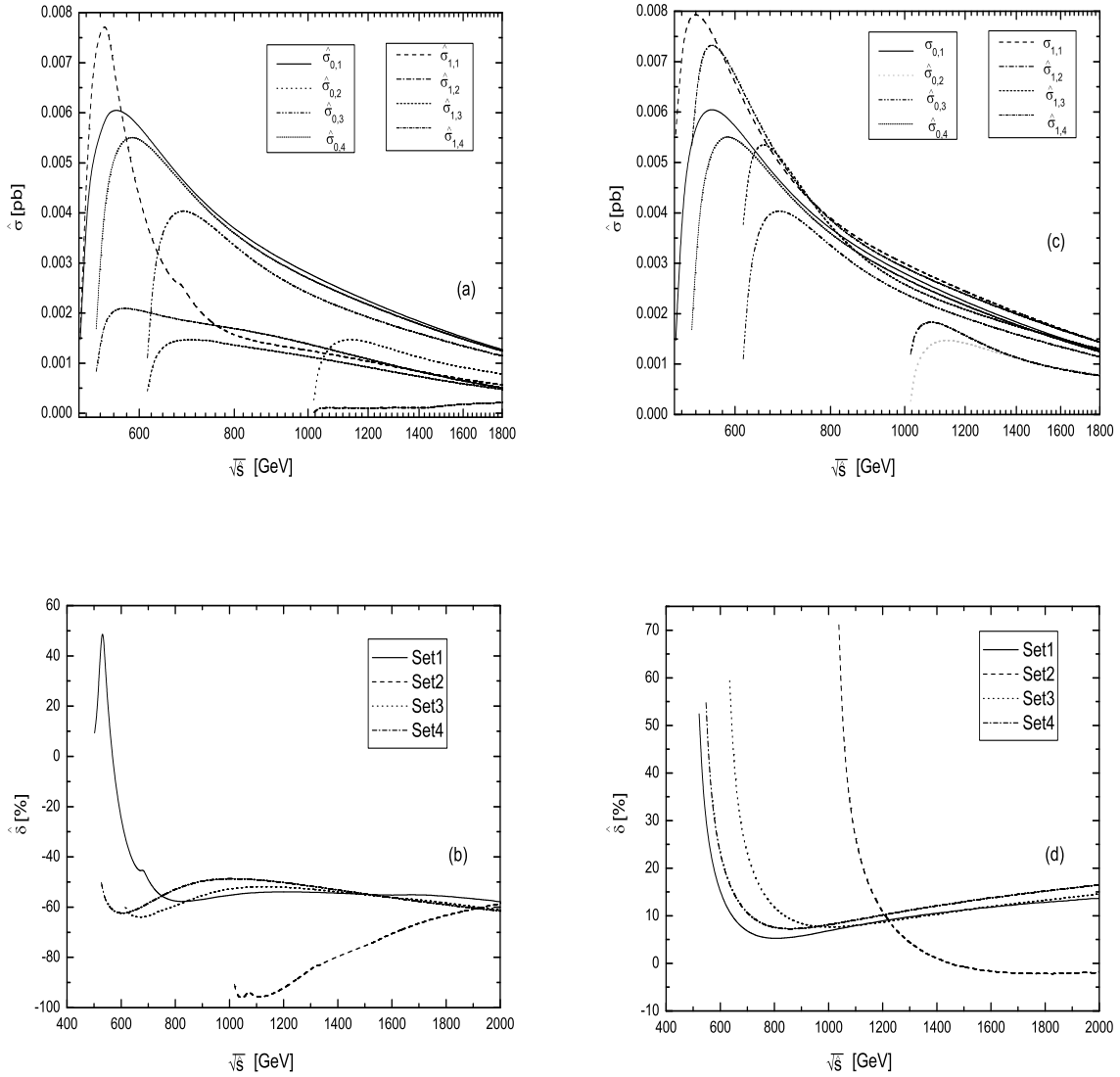


Figure 9: (a) The Born and full $\mathcal{O}(\alpha_{ew})$ EW corrected cross sections for the $\gamma\gamma \rightarrow \tilde{b}_2\bar{\tilde{b}}_2$ subprocess as the functions of c.m.s. energy \sqrt{s} with four data sets, respectively. (b) The full $\mathcal{O}(\alpha_{ew})$ EW relative corrections to $\gamma\gamma \rightarrow \tilde{b}_2\bar{\tilde{b}}_2$ subprocess. (c) The Born and full $\mathcal{O}(\alpha_s)$ QCD corrected cross sections for the $\gamma\gamma \rightarrow \tilde{b}_2\bar{\tilde{b}}_2$ subprocess as the functions of c.m.s. energy \sqrt{s} with four data sets, respectively. (d) The full $\mathcal{O}(\alpha_s)$ QCD relative correction to $\gamma\gamma \rightarrow \tilde{b}_2\bar{\tilde{b}}_2$ subprocess.

corrections in the region near the threshold energy of the $\tilde{b}_1\bar{\tilde{b}}_1$ pair production are extremely large, these values are untrustworthy due to the non-perturbative QCD effects. The values of the relative $\mathcal{O}(\alpha_s)$ QCD corrections at the position of $\sqrt{\hat{s}} = 2000$ GeV, are 23.1%, 13.4%, 21.5% and 28.7%, for *Set1*, *Set2*, *Set3* and *Set4* respectively.

The full $\mathcal{O}(\alpha_{ew})$ EW and $\mathcal{O}(\alpha_s)$ QCD corrected cross sections for the $\gamma\gamma \rightarrow \tilde{b}_2\bar{\tilde{b}}_2$ subprocess are depicted in Fig.9(a) and Fig.9(c) separately, while their corresponding relative corrections are plotted in Fig.9(b) and Fig.9(d) respectively. Although the line-shapes in Fig.9(a) and Fig.9(c) are similar with the corresponding ones in Fig.8(a) and (c) for the $\tilde{b}_1\bar{\tilde{b}}_1$ pair production, the values of the corrected cross section in Fig.9(a) and Fig.9(c) are much smaller due to $m_{\tilde{b}_2} > m_{\tilde{b}_1}$. Nevertheless, Fig.9(b) shows that when $\sqrt{\hat{s}}$ is large enough, the absolute EW relative corrections to $\gamma\gamma \rightarrow \tilde{b}_2\bar{\tilde{b}}_2$ approach about 50% or beyond for all four data sets. The peak at the position of $\sqrt{\hat{s}} \sim 525$ GeV for *Set1* in Fig.9(b) comes from the resonance effect of $\sqrt{\hat{s}} \sim 2m_{H^+}$. We find also from Fig.9(d) that the absolute QCD relative corrections to the $\gamma\gamma \rightarrow \tilde{b}_2\bar{\tilde{b}}_2$ subprocess are generally comparable with the EW corrections or even smaller than EW ones, especially in the large colliding energy region.

In the following discussion, we present some numerical results about the parent process $e^+e^- \rightarrow \gamma\gamma \rightarrow \tilde{f}_i\bar{\tilde{f}}_i$ ($i = \tau, t, b$, $i = 1, 2$). For convenience, we denote the cross sections of the parent process $e^+e^- \rightarrow \gamma\gamma \rightarrow \tilde{f}_i\bar{\tilde{f}}_i$ containing the $\mathcal{O}(\alpha_{ew})$ EW and $\mathcal{O}(\alpha_s)$ QCD corrections as

$$\sigma^{EW} = \sigma_0 + \Delta\sigma^{EW} = \sigma_0(1 + \delta^{EW}), \quad \sigma^{QCD} = \sigma_0 + \Delta\sigma^{QCD} = \sigma_0(1 + \delta^{QCD})$$

where δ^{EW} and δ^{QCD} are the $\mathcal{O}(\alpha_{ew})$ EW and $\mathcal{O}(\alpha_s)$ QCD relative correction respectively. In the following numerical calculations, we take the input parameters of higgsino-like data *Set3*, but let M_{SUSY} running from 200 GeV to 400 GeV. Fig.10(a) and Fig.10(c) show the Born and full $\mathcal{O}(\alpha_{ew})$ EW corrected cross sections for the $e^+e^- \rightarrow \gamma\gamma \rightarrow \tilde{\tau}_1\bar{\tilde{\tau}}_1$ and $e^+e^- \rightarrow \gamma\gamma \rightarrow \tilde{\tau}_2\bar{\tilde{\tau}}_2$ process as the functions of the soft-breaking sfermion mass M_{SUSY} . In Fig.10(a), the solid and dashed curves correspond to Born and full $\mathcal{O}(\alpha_{ew})$ EW corrected cross sections for $\sqrt{s} = 500$ GeV, 800 GeV, 1000 GeV, 2000 GeV, respectively. It is obvious that all the curves for the Born and EW corrected cross sections decrease rapidly as M_{SUSY} going up from 200 to 400 GeV, but the damping decrement is getting smaller with the increment of the colliding energy \sqrt{s} . We can read from Fig.10(a) that the values of the EW corrected cross sections decrease from 28.3 fb, 98.9 fb, 110 fb and 92.8 fb to 2.25 fb, 0.1 fb, 1.28 fb and 20.8 fb for $\sqrt{s} = 500$ GeV, 800 GeV, 1000 GeV, 2000 GeV respectively, when M_{SUSY} increases from 200 GeV to 400 GeV. In Fig.10(c), the curves show the Born and $\mathcal{O}(\alpha_{ew})$ EW corrected cross sections for $e^+e^- \rightarrow \gamma\gamma \rightarrow \tilde{\tau}_2\bar{\tilde{\tau}}_2$ process with $\sqrt{s} = 800$ GeV, 1000 GeV, 2000 GeV respectively. All the curves have the analogous tendency as the curves in Fig.10(a). The values of the corrected cross sections in Fig.10(c) are smaller than those for $e^+e^- \rightarrow \gamma\gamma \rightarrow \tilde{\tau}_1\bar{\tilde{\tau}}_1$ in Fig.10(a). The EW relative corrections to the $e^+e^- \rightarrow \gamma\gamma \rightarrow \tilde{\tau}_1\bar{\tilde{\tau}}_1$ process as the functions of M_{SUSY} are depicted in Fig.10(b) for $\sqrt{s} = 500$ GeV, 800 GeV, 1000 GeV and 2000 GeV. From this figure, we can see that in the range of $M_{SUSY} = 200$ GeV to 400 GeV, this relative correction can reach -5.46% at the position of $M_{SUSY} = 340$ GeV when we take $\sqrt{s} = 800$ GeV. If we take e^+e^- colliding energy $\sqrt{s} = 2$ TeV, we can get -18.69% relative correction to $e^+e^- \rightarrow \gamma\gamma \rightarrow \tilde{\tau}_1\bar{\tilde{\tau}}_1$ process when $M_{SUSY} = 400$ GeV. Fig.10(d) displays the EW relative corrections to $e^+e^- \rightarrow \gamma\gamma \rightarrow \tilde{\tau}_2\bar{\tilde{\tau}}_2$ process. We can see from this figure that the numerical values of these relative corrections increase rapidly from -16.43% to -3.56% when M_{SUSY}

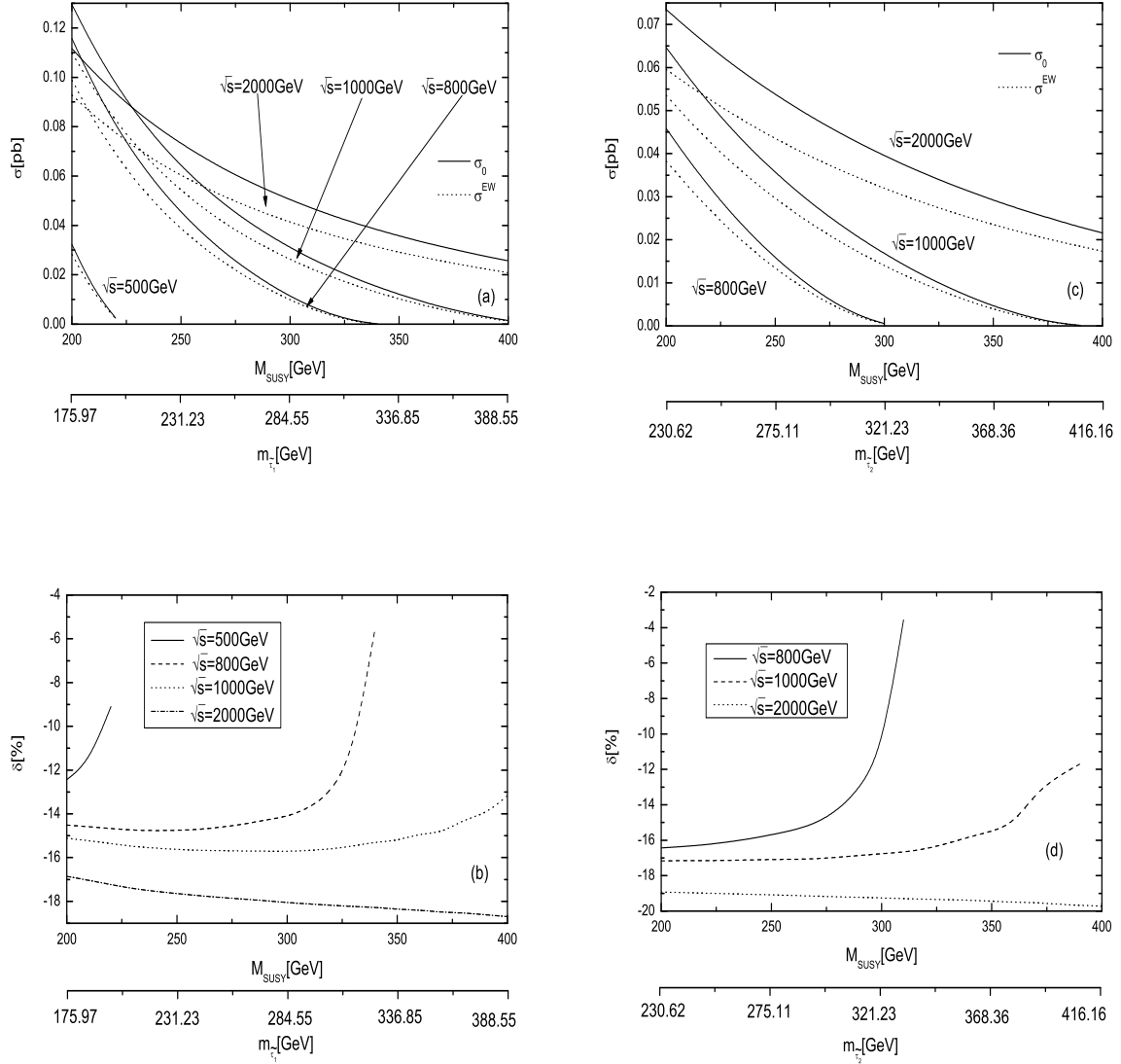


Figure 10: (a) The Born and full $\mathcal{O}(\alpha_{ew})$ EW corrected cross sections for the $e^+e^- \rightarrow \gamma\gamma \rightarrow \tilde{\tau}_1\tilde{\tau}_1^*$ process as functions of the soft-breaking sfermion mass M_{SUSY} with $\sqrt{s} = 500$ GeV, 800 GeV, 1000 GeV, 2000 GeV, respectively. (b) The full $\mathcal{O}(\alpha_{ew})$ EW relative corrections to the $e^+e^- \rightarrow \gamma\gamma \rightarrow \tilde{\tau}_1\tilde{\tau}_1^*$ process as the functions of M_{SUSY} with $\sqrt{s} = 500$ GeV, 800 GeV, 1000 GeV, 2000 GeV, respectively. (c) The Born and full $\mathcal{O}(\alpha_{ew})$ EW corrected cross sections for the $e^+e^- \rightarrow \gamma\gamma \rightarrow \tilde{\tau}_2\tilde{\tau}_2^*$ process as functions of the soft-breaking sfermion mass M_{SUSY} with $\sqrt{s} = 500$ GeV, 800 GeV, 1000 GeV, 2000 GeV, respectively. (d) The full $\mathcal{O}(\alpha_{ew})$ EW relative corrections to the $e^+e^- \rightarrow \gamma\gamma \rightarrow \tilde{\tau}_2\tilde{\tau}_2^*$ process as the functions of M_{SUSY} with $\sqrt{s} = 500$ GeV, 800 GeV, 1000 GeV, 2000 GeV, respectively.

goes up from 200 GeV to 310 GeV for $\sqrt{s} = 800$ GeV, and from -17.16% to -11.7% when M_{SUSY} increases from 200 GeV to 390 GeV for $\sqrt{s} = 1000$ GeV. But for $\sqrt{s} = 2000$ GeV the value of δ^{EW} is relative stable and keeps in the range of [-18.93%, -19.72%] as M_{SUSY} varying from 200 GeV to 400 GeV.

The numerical results for the process $e^+e^- \rightarrow \gamma\gamma \rightarrow \tilde{t}_1\bar{\tilde{t}}_1$ are plotted in Fig.11. Fig.11(a) and Fig.11(c) display the Born and full one-loop EW and QCD corrected cross sections as the functions of M_{SUSY} with $\sqrt{s} = 500$ GeV, 800 GeV, 1000 GeV, 2000 GeV, respectively. As we expect, the curves in Fig.11(a) for the cross sections in Born approximation and at $\mathcal{O}(\alpha_{ew})$ EW one-loop level, have some similar behaviors with those for the $\tilde{\tau}_1\bar{\tilde{\tau}}_1$ production process shown in Fig.10(a). We can find from Fig.11(a) that the full $\mathcal{O}(\alpha_{ew})$ EW corrected cross sections decrease from 87.3 fb and 65.3 fb to 1.21 fb and 11.8 fb when M_{SUSY} goes from 200 GeV to 400 GeV for $\sqrt{s} = 1000$ GeV, 2000 GeV, respectively. In Fig.11(c) the solid and dotted curves correspond to the Born and one-loop QCD corrected cross sections versus M_{SUSY} with $\sqrt{s} = 500$ GeV, 800 GeV, 1000 GeV, 2000 GeV, respectively. From this figure, we can see that the value of the QCD corrected cross section reaches 118 fb for $\sqrt{s} = 1000$ GeV with our chosen parameters. In order to study the EW and QCD radiative corrections more clearly, we plot the EW and QCD relative corrections to the $e^+e^- \rightarrow \gamma\gamma \rightarrow \tilde{t}_1\bar{\tilde{t}}_1$ process in Fig.11(b) and Fig.11(d). In Fig.11(b), the resonance effect at the position of $M_{SUSY} = 386$ GeV is due to the condition of $m_{\tilde{t}_1} \sim m_t + m_{\tilde{\chi}_1^0}$. Fig.11(b) shows the EW relative corrections for $\sqrt{s} = 1000$ GeV and 2000 GeV can reach -27.15% and -26.78% at the position of $M_{SUSY} = 400$ GeV. From Fig.11(d) we find the curves for $\sqrt{s} = 500$ GeV, 800 GeV and 1000 GeV go up fleetly with the increment of M_{SUSY} , but for the curve of $\sqrt{s} = 2000$ GeV the relative correction is almost stable, varying in the range of [14.6%, 13.3%].

The results for $e^+e^- \rightarrow \gamma\gamma \rightarrow \tilde{t}_2\bar{\tilde{t}}_2$ are represented in Fig.12. Fig.12(a) shows the plot of the Born and full one-loop EW corrected cross sections versus M_{SUSY} . Fig.12(b) describes the EW relative corrections as the functions of M_{SUSY} . The QCD corrected cross sections and QCD relative corrections are plotted in Fig.12(c) and Fig.12(d), respectively. In Fig.12(a) the EW corrected cross section of $e^+e^- \rightarrow \gamma\gamma \rightarrow \tilde{t}_2\bar{\tilde{t}}_2$ process decreases from 13.2 fb to 5.3 fb for $\sqrt{s} = 2000$ GeV, when M_{SUSY} increases from 200 GeV to 400 GeV. At the position of $M_{SUSY} = 266$ GeV in Fig.12(a), there is a dithering on the curve of $\sqrt{s} = 2000$ GeV, which is due to resonance effect of $m_{\tilde{t}_2} \sim m_t + m_{\tilde{\chi}_2^0}$. The resonance effect on the EW relative correction curves at the position near $M_{SUSY} = 266$ GeV is also shown in Fig.12(b). In Fig.12(d), the QCD relative corrections for $\sqrt{s} = 1000$ GeV are rather larger and vary in the region between 36.4% and 76.1% with the increment of M_{SUSY} , but the QCD relative corrections for $\sqrt{s} = 2000$ GeV are smaller, and have the values in the range between 15.5% and 18.6%.

We also present the results of the $e^+e^- \rightarrow \gamma\gamma \rightarrow \tilde{b}_1\bar{\tilde{b}}_1$ process in Fig.13. Fig.13(a) and Fig.13(c) show the Born and full one-loop EW and QCD corrected cross sections, respectively. In Fig.13(a) and Fig.13(c) we find that all the curves of cross sections at the Born level and involving EW and QCD one-loop contributions, decrease with the increment of the M_{SUSY} . For example, when M_{SUSY} varies from 200 to 400 GeV, the two curves of the cross sections including full one-loop EW corrections for $\sqrt{s} = 1000$ GeV and 2000 GeV in Fig.13(a), goes down from 11.1 fb and 6.6 fb to 0.13 fb and 0.65 fb respectively. While the two curves in Fig.13(c), which represent the cross sections including QCD corrections for $\sqrt{s} = 1000$ GeV and 2000 GeV, decrease from 12.8 fb and 8.4 fb to 0.3 fb and 1.3 fb, respectively. Fig.13(b)

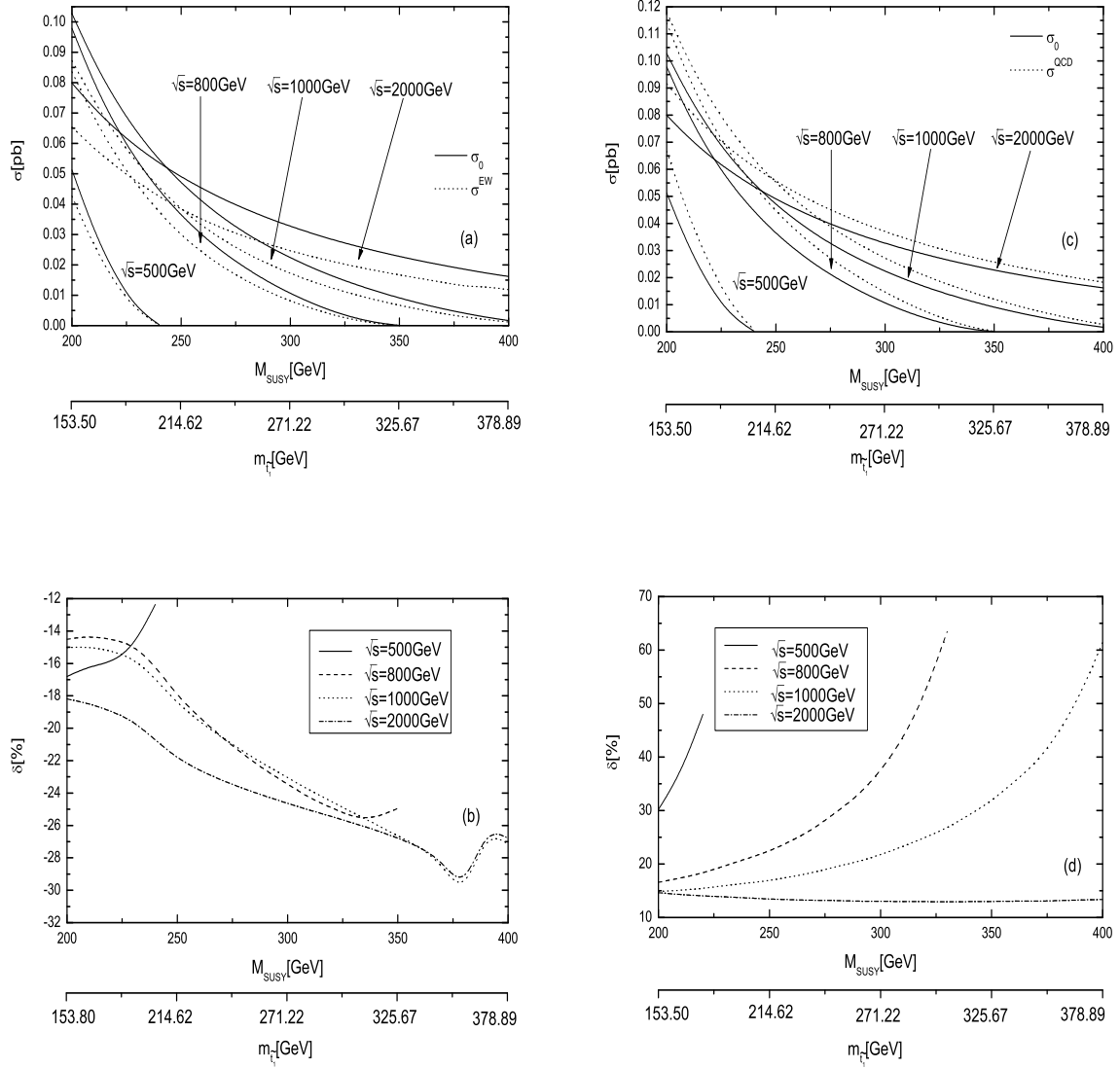


Figure 11: (a) The Born and full $\mathcal{O}(\alpha_{ew})$ EW corrected cross sections for the $e^+e^- \rightarrow \gamma\gamma \rightarrow \tilde{t}_1\tilde{t}_1$ process as the functions of the soft-breaking sfermion mass M_{SUSY} with $\sqrt{s} = 500, 800, 1000, 2000$ GeV, respectively. (b) The full $\mathcal{O}(\alpha_{ew})$ EW relative corrections to the $e^+e^- \rightarrow \gamma\gamma \rightarrow \tilde{t}_1\tilde{t}_1$ process as the functions of M_{SUSY} with $\sqrt{s} = 500$ GeV, 800 GeV, 1000 GeV, 2000 GeV, respectively. (c) The Born and full $\mathcal{O}(\alpha_s)$ QCD corrected cross sections for the $e^+e^- \rightarrow \gamma\gamma \rightarrow \tilde{t}_1\tilde{t}_1$ process as the functions of the soft-breaking sfermion mass M_{SUSY} with $\sqrt{s} = 500, 800, 1000, 2000$ GeV, respectively. (d) The full $\mathcal{O}(\alpha_s)$ QCD relative corrections to the $e^+e^- \rightarrow \gamma\gamma \rightarrow \tilde{t}_1\tilde{t}_1$ process as the functions of M_{SUSY} with $\sqrt{s} = 500$ GeV, 800 GeV, 1000 GeV, 2000 GeV, respectively.

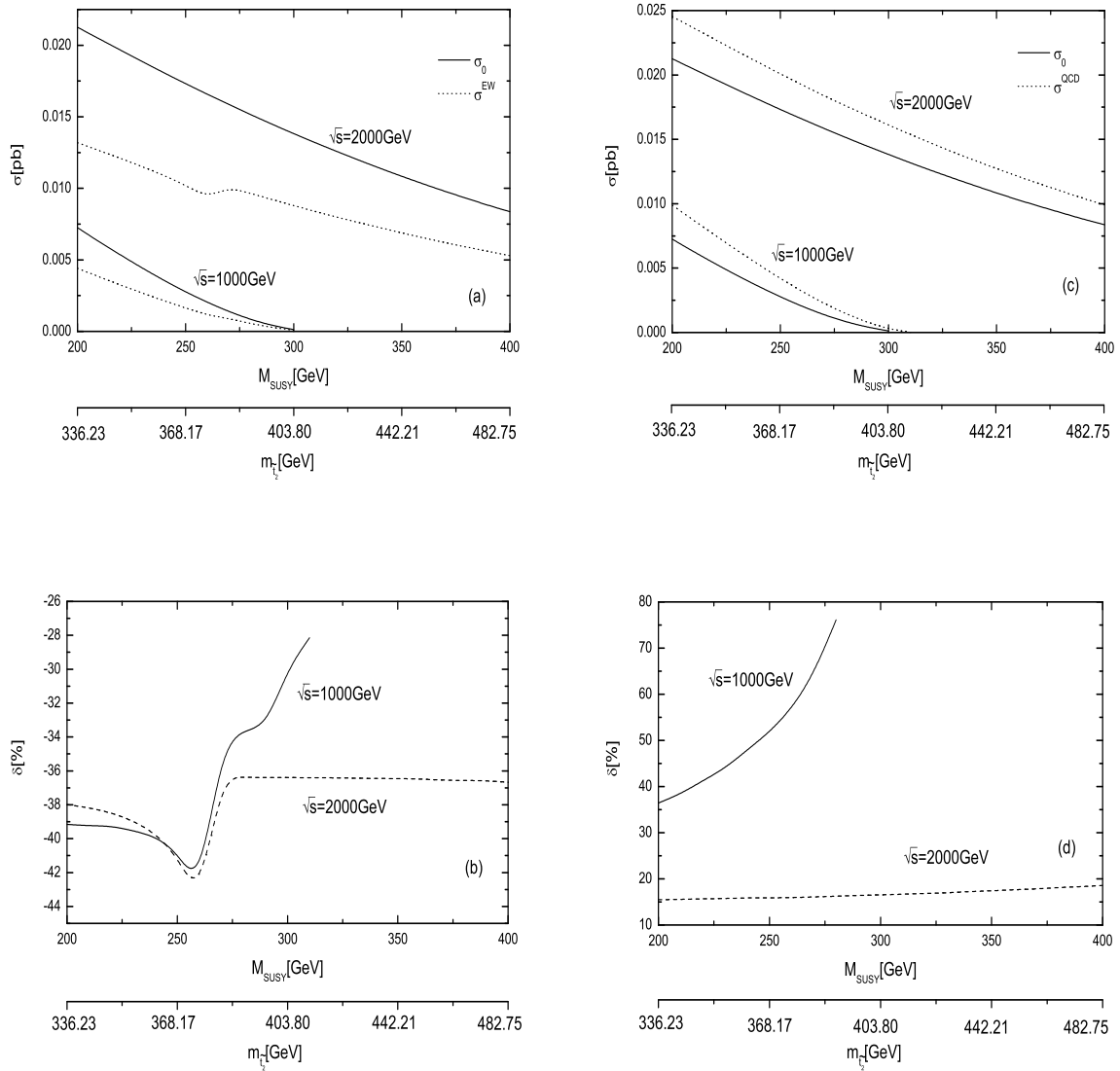


Figure 12: (a) The Born and full $\mathcal{O}(\alpha_{ew})$ EW corrected cross sections for the $e^+e^- \rightarrow \gamma\gamma \rightarrow \tilde{t}_2\tilde{t}_2$ process as the functions of the soft-breaking sfermion mass M_{SUSY} with $\sqrt{s} = 1000$ GeV, 2000 GeV, respectively. (b) The full $\mathcal{O}(\alpha_{ew})$ EW relative corrections to the $e^+e^- \rightarrow \gamma\gamma \rightarrow \tilde{t}_2\tilde{t}_2$ process as the functions of M_{SUSY} with $\sqrt{s} = 1000$ GeV, 2000 GeV, respectively. (c) The Born and full $\mathcal{O}(\alpha_s)$ QCD corrected cross sections for the $e^+e^- \rightarrow \gamma\gamma \rightarrow \tilde{t}_2\tilde{t}_2$ process as functions of the soft-breaking sfermion mass M_{SUSY} with $\sqrt{s} = 1000$ GeV, 2000 GeV, respectively. (d) The full $\mathcal{O}(\alpha_s)$ QCD relative corrections to the $e^+e^- \rightarrow \gamma\gamma \rightarrow \tilde{t}_2\tilde{t}_2$ process as the functions of M_{SUSY} with $\sqrt{s} = 1000$ GeV, 2000 GeV, respectively.

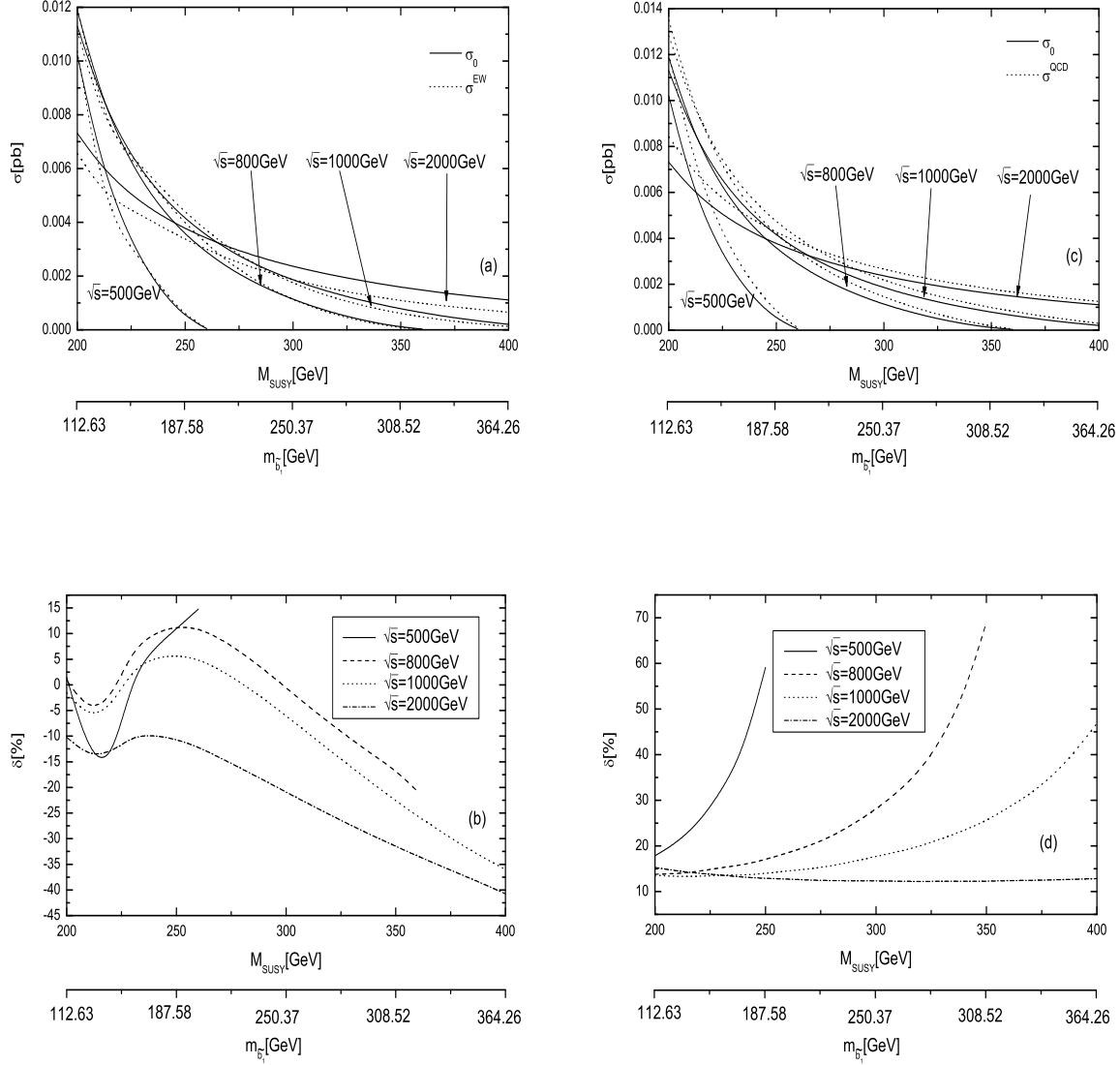


Figure 13: (a) The Born and full $\mathcal{O}(\alpha_{ew})$ EW corrected cross sections for the $e^+e^- \rightarrow \gamma\gamma \rightarrow \tilde{b}_1\bar{\tilde{b}}_1$ process as the functions of the soft-breaking sfermion mass M_{SUSY} with $\sqrt{s} = 500$ GeV, 800 GeV, 1000 GeV, 2000 GeV, respectively. (b) The full $\mathcal{O}(\alpha_{ew})$ EW relative corrections to the $e^+e^- \rightarrow \gamma\gamma \rightarrow \tilde{b}_1\bar{\tilde{b}}_1$ process as the functions of M_{SUSY} with $\sqrt{s} = 500$ GeV, 800 GeV, 1000 GeV, 2000 GeV, respectively. (c) The Born and full $\mathcal{O}(\alpha_s)$ QCD corrected cross sections for the $e^+e^- \rightarrow \gamma\gamma \rightarrow \tilde{b}_1\bar{\tilde{b}}_1$ process as the functions of the soft-breaking sfermion mass M_{SUSY} with $\sqrt{s} = 500$ GeV, 800 GeV, 1000 GeV, 2000 GeV, respectively. (d) The full $\mathcal{O}(\alpha_s)$ QCD relative corrections to the $e^+e^- \rightarrow \gamma\gamma \rightarrow \tilde{b}_1\bar{\tilde{b}}_1$ process as the functions of M_{SUSY} with $\sqrt{s} = 500$ GeV, 800 GeV, 1000 GeV, 2000 GeV, respectively.

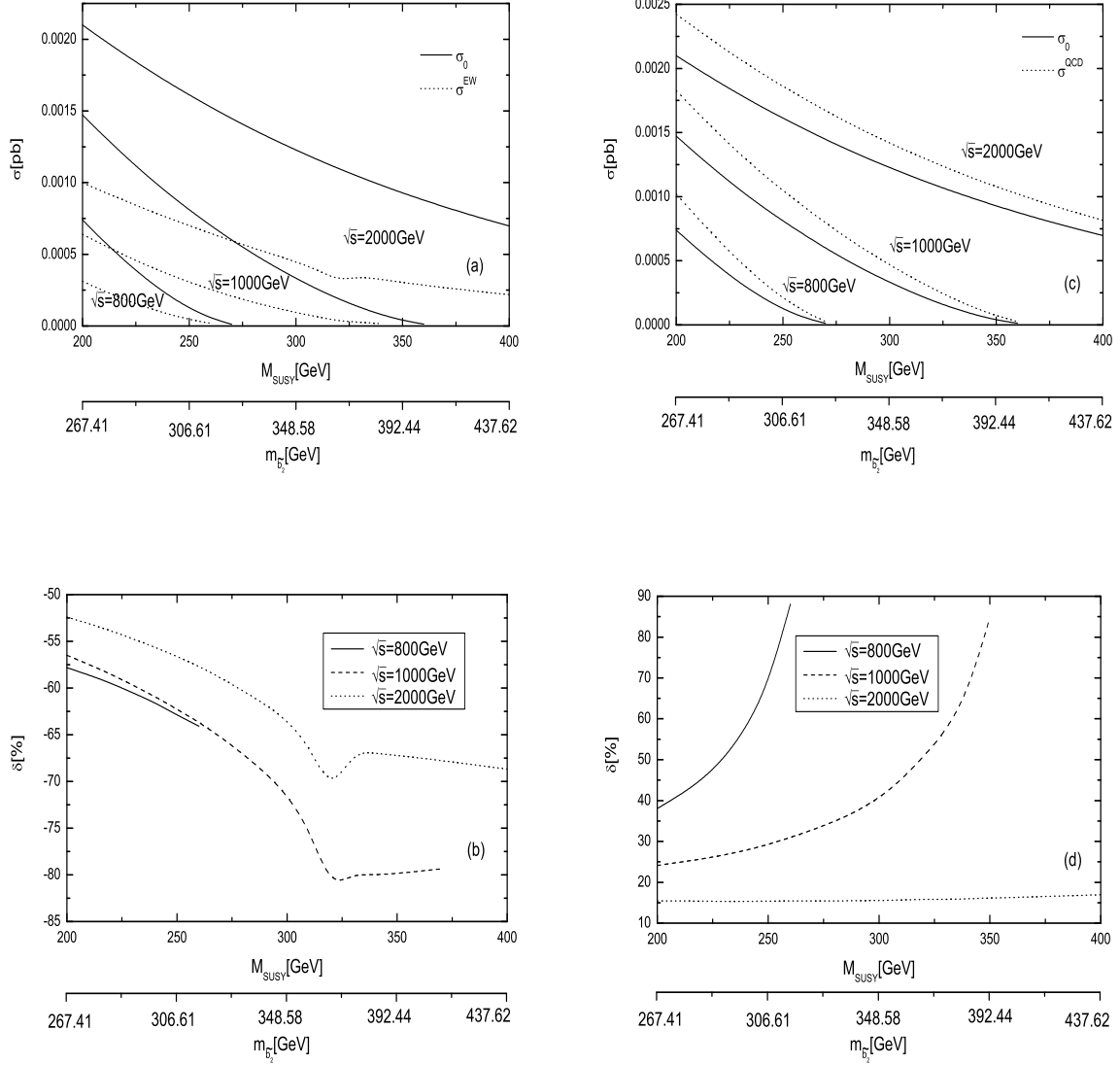


Figure 14: (a) The Born and full $\mathcal{O}(\alpha_{ew})$ EW corrected cross sections for the $e^+e^- \rightarrow \gamma\gamma \rightarrow \tilde{b}_2\tilde{b}_2$ process as the functions of the soft-breaking sfermion mass M_{SUSY} with $\sqrt{s} = 800$ GeV, 1000 GeV, 2000 GeV, respectively. (b) The full $\mathcal{O}(\alpha_{ew})$ EW relative corrections to the $e^+e^- \rightarrow \gamma\gamma \rightarrow \tilde{b}_2\tilde{b}_2$ process as the functions of M_{SUSY} with $\sqrt{s} = 800$ GeV, 1000 GeV, 2000 GeV, respectively. (c) The Born and full $\mathcal{O}(\alpha_s)$ QCD corrected cross sections for the $e^+e^- \rightarrow \gamma\gamma \rightarrow \tilde{b}_2\tilde{b}_2$ process as the functions of the soft-breaking sfermion mass M_{SUSY} with $\sqrt{s} = 800$ GeV, 1000 GeV, 2000 GeV, respectively. (d) The full $\mathcal{O}(\alpha_s)$ QCD relative corrections to the $e^+e^- \rightarrow \gamma\gamma \rightarrow \tilde{b}_2\tilde{b}_2$ process as the functions of M_{SUSY} with $\sqrt{s} = 800$ GeV, 1000 GeV, 2000 GeV, respectively.

shows the full one-loop EW relative corrections to the $e^+e^- \rightarrow \gamma\gamma \rightarrow \tilde{b}_1\bar{\tilde{b}}_1$ process, as the functions of M_{SUSY} for $\sqrt{s} = 500, 800, 1000, 2000$ GeV respectively. We see that there occur the resonance effects on each curve at the position of $m_{\tilde{b}_1} \sim m_{H^+} - m_{\tilde{t}_1} \sim 133$ GeV (corresponding to $M_{SUSY} \sim 212$ GeV). Fig.13(d) displays the full one-loop QCD relative corrections as the functions of M_{SUSY} with $\sqrt{s} = 500, 800, 1000, 2000$ GeV, respectively. The QCD relative corrections can be rather larger for $\sqrt{s} = 500$ GeV and 800 GeV, and can reach 59% and 69% at the positions of $M_{SUSY} = 250$ GeV and 350 GeV, respectively.

Finally, we present the Born and full one-loop EW and QCD corrections to $e^+e^- \rightarrow \gamma\gamma \rightarrow \tilde{b}_2\bar{\tilde{b}}_2$ process in Fig.14. Comparing Fig.14(a) with Fig.13(a), we can see that the Born and full one-loop EW corrected cross sections for $\tilde{b}_2\bar{\tilde{b}}_2$ pair production are smaller than the corresponding ones for $\tilde{b}_1\bar{\tilde{b}}_1$ pair production because of $m_{\tilde{b}_2} > m_{\tilde{b}_1}$. But the EW relative corrections to $e^+e^- \rightarrow \gamma\gamma \rightarrow \tilde{b}_2\bar{\tilde{b}}_2$ process are rather large and can be comparable with their QCD corrections as shown in Fig.14(b) and Fig.14(d). We can also find that when $M_{SUSY} = 200$ GeV, the EW relative corrections are -57.8% (for $\sqrt{s} = 800$ GeV), -56.5% (for $\sqrt{s} = 1000$ GeV) and -52.4% (for $\sqrt{s} = 2000$ GeV), and when $M_{SUSY} = 200$ GeV the QCD relative corrections are 38.1% and 24.1% for $\sqrt{s} = 800$ GeV and 1000 GeV respectively, but for $\sqrt{s} = 2000$ GeV the QCD relative correction varies in the a small range of [15.4%, 16.9%].

4 Summery

In this paper, we have calculated the full $\mathcal{O}(\alpha_{ew})$ EW and $\mathcal{O}(\alpha_s)$ QCD contributions to the third generation scalar fermion ($\tilde{\tau}_i, \tilde{t}_i, \tilde{b}_i, i = 1, 2$) pair production in $\gamma\gamma$ collision at an e^+e^- collider. The calculation of the radiative corrections was carried out analytically and numerically. The numerical results were discussed in conditions of both gaugino-like and higgsino-like input parameter scenarios. Our investigation shows that the full $\mathcal{O}(\alpha_{ew})$ EW relative corrections to both subprocesses and parent processes are typically of the order 10~30%, and the EW relative corrections to the squark pair production can be comparable with the $\mathcal{O}(\alpha_s)$ QCD contributions in some parameter space, especially in high $\gamma\gamma$ and e^+e^- colliding energy regions. For example, the EW relative corrections can reach -50% and -40.76% at $\sqrt{\hat{s}}(\sqrt{s}) = 2000$ GeV to the subprocess $\gamma\gamma \rightarrow \tilde{b}_1\bar{\tilde{b}}_1$ and its parent process $e^+e^- \rightarrow \gamma\gamma \rightarrow \tilde{b}_1\bar{\tilde{b}}_1$, respectively. We find the full $\mathcal{O}(\alpha_s)$ QCD corrections to these squark pair production subprocesses are also large under our input data sets, for example, the QCD relative correction is 28.7% for $\gamma\gamma \rightarrow \tilde{b}_1\bar{\tilde{b}}_1$ subprocess with $\sqrt{s} = 2000$ GeV and *Set4* parameters. In conclusion, our numerical results have indicated that the full $\mathcal{O}(\alpha_{ew})$ EW corrections to $e^+e^- \rightarrow \gamma\gamma \rightarrow \tilde{f}_i\bar{\tilde{f}}_i$ ($f = t, b, \tau, i = 1, 2$) processes and $\mathcal{O}(\alpha_s)$ QCD corrections to $e^+e^- \rightarrow \gamma\gamma \rightarrow \tilde{q}_i\bar{\tilde{q}}_i$ ($q = t, b, i = 1, 2$) processes, give substantial contributions in some parameter space. Therefore, these radiative corrections cannot be neglected in considering the third generation sfermion pair productions in $\gamma\gamma$ collision mode at future linear colliders.

Acknowledgments:

This work was supported in part by the National Natural Science Foundation of China and special fund sponsored by China Academy of Science.

References

- [1] J. Ellis and S. Rudaz, Phys. Lett. B128(1983)248; J.F. Gunion and H.E. Haber, Nucl. Phys. B272(1986)1.
- [2] C. Adolphsen *et al.*, (International Study Group Collaboration), ‘International study group progress report on linear collider development’, SLAC-R-559 and KEK-REPORT-2000-7 (April, 2000).
- [3] N. Akasaka *et al.*, ‘JLC design study’, KEK-REPORT-97-1.
- [4] R. Brinkmann, K. Flottmann, J. Rossbach, P. Schmuser, N. Walker and H. Weise(editor), ‘TESLA: The superconducting electron positron linear collider with an integrated X-ray laser laboratory. Technical design report, Part 2: The Accelerator’, DESY-01-11 (March, 2001).
- [5] ‘A 3 TeV e^+e^- Linear Collider Based on CLIC Technology’, G. Guignard(editor), CERN-2000-008.
- [6] A. Freitas, A. von Manteuffel, P. M. Zerwas, Eur.Phys.J. C34 (2004) 487-512.
- [7] K. Huitu, J. Maalampi, M. Raidal, Phys.Lett. B328 (1994) 60-66.
- [8] Howard Baer, B. W. Harris, Mary Hall Reno, Phys.Rev. D57 (1998) 5871-5874.
- [9] A. Freitas, D. J. Miller, eConf C010630 (2001) E3061.
- [10] K.I. Hikasa and M. Kobayashi, Phys. Rev. D36(1987)724.
- [11] W. Beenakker, R. Hopker and P.M. Zerwas, Phys. Lett. B349(1995)463; A. Arhrib, M. Capdequi-Peyranere and A. Djouadi, Phys. Rev D52(1995)1404; H. Eberl, A. Bartl and W. Majerotto, Nucl.Phys. B472(1996)481, hep-ph/9603206.
- [12] C.H. Chang, L. Han, W.G. Ma and Z.H. Yu, Nucl.Phys. B515 (1998) 15-33.
- [13] K. Kovařík, C. Weber, H. Eberl, W. Majerotto, Phys.Lett. B591 (2004) 242-254.
- [14] A. Arhrib, W. Hollik, JHEP 0404 (2004) 073.
- [15] I.F. Ginzbyrg, G.L. Kotkin, V.G. Serbo and V.I. Telnov, Pis’ma ZHETF 34 (1981)514; Nucl. Instr. Methods 205 (1983)47.
- [16] Frank Cuypers (MPI Munich), talk presented at the International Europhysics Conference on High Energy Physics, Brussels, 27/7-2/8,1995, MPI-PhT/95-93, hep-ph/9509400;
- [17] G.’t Hooft and M. Veltman, Nucl. Phys. B153, 365 (1979).
- [18] I.F. Ginzburg, G.L. Kotkin, V.G. Serbo and V.I. Telnov, Nucl. Instr. Methods 205 (1983) 47; L. Han, C.G. Hu, C.S. Li and W.G. Ma, Phys. Rev. D54(1996)2363.
- [19] A. Denner, Fortschr. Phys. 41, 307 (1993).

- [20] T. Hahn, Comp. Phys. Commun. **140**, 418 (2001).
- [21] W.T. Giele and E.W.N. Glover, Phys. Rev. **D46**, 1980 (1992); W.T. Giele, E.W. Glover and D.A. Kosower, Nucl. Phys. **B403**, 633 (1993); S. Keller and E. Laenen, Phys. Rev. **D59**, 114004 (1999).
- [22] G.'t Hooft and M. Veltman, Nucl. Phys. **B153**, 365 (1979).
- [23] I. Ginzburg, G. Kotkin, V. Serbo and V. Telnov, Pizma ZhETF, **34** (1981) 514; JETP Lett. **34** (1982) 491. Preprint INP 81-50, 1981, Novosibirsk.
- [24] I. Ginzburg, G. Kotkin, V. Serbo and V. Telnov, Nucl. Instr. & Meth. **205** (1983) 47, Preprint INP 81-102, 1991, Novosibirsk.
- [25] I. Ginzburg, G. Kotkin, S. Panfil, V. Serbo and V. Telnov, Nucl. Instr. & Meth. **219** (1984) 5.
- [26] K. Cheung, Phys.Rev. **D47**(1993)3750.
- [27] R. Blankenbecler and S.D.Drell, Phys. Rev. Lett. 61(1988)2324; F. Halzen, C.S. Kim and M.L. Stong, Phys. Lett. B274(1992)489; M. Drees and R.M. Godbole, Phys. Lett. 67(1991)1189.
- [28] V. Telnov, Nucl. Instr. Methods A294(1990)72.
- [29] V. Telnov, Nucl. Instrum. Methods Phys. Res. **A294**(1990)72; L. Ginzburg, G. Kotkin and H. Spiesberger, Fortschr. Phys. **34**(1986)687.
- [30] J. F. Gunion, H. E. Haber, Nucl. Phys. **B272** (1986) 1.
- [31] S. Eidelman, *et al.*, Phys. Lett. **B592**(2004)1.
- [32] F. Jegerlehner, DESY 01-029, hep-ph/0105283.
- [33] C. Weber, H. Eberl, W. Majerotto, Phys. Lett. **B572**(2003) 56, hep-ph/0305250.
- [34] H. Eberl, M. Kincel, W. Majerotto and Y. Yamada, Nucl. Phys. **B625**(2002) 372, hep-ph/0111303.
- [35] Thomas Hahn and Christian Schappacher, Comput.Phys.Commun. 143(2002)54-68, hep-ph/0105349.

Figure Captions

Figure 1 The lowest order Feynman diagrams for the subprocess $\gamma\gamma \rightarrow \tilde{f}_i \bar{\tilde{f}}_i$ ($f = \tau, t, b$).

Figure 2 The real photon emission diagrams for the process $\gamma\gamma \rightarrow \tilde{f}_i \bar{\tilde{f}}_i \gamma$ ($f = \tau, t, b$).

Figure 3 The real gluon emission diagrams for the process $\gamma\gamma \rightarrow \tilde{q}_i \bar{\tilde{q}}_i g$ ($q = t, b$).

Figure 4 The full $\mathcal{O}(\alpha_s)$ QCD corrections to $\gamma\gamma \rightarrow \tilde{t}_1 \bar{\tilde{t}}_1$ as a function of the soft gluon cutoff $\Delta E_g/E_b$ in conditions of $\sqrt{\hat{s}} = 500$ GeV and *Set1* parameters.

Figure 5(a) The Born and full $\mathcal{O}(\alpha_{ew})$ EW corrected cross sections for the $\gamma\gamma \rightarrow \tilde{\tau}_1\tilde{\tau}_1$ subprocess as the functions of c.m.s. energy of $\gamma\gamma$ collider $\sqrt{\hat{s}}$ with four different data sets, respectively.

Figure 5(b) The full $\mathcal{O}(\alpha_{ew})$ EW relative correction to the $\gamma\gamma \rightarrow \tilde{\tau}_1\tilde{\tau}_1$ subprocess. The solid, dashed, dotted and dash-dotted curves correspond to four different data set cases, respectively.

Figure 5(c) The Born and full $\mathcal{O}(\alpha_{ew})$ EW corrected cross sections for the $\gamma\gamma \rightarrow \tilde{\tau}_2\tilde{\tau}_2$ subprocess as the functions of c.m.s. energy of $\gamma\gamma$ collider $\sqrt{\hat{s}}$ with four different data sets, respectively.

Figure 5(d) The full $\mathcal{O}(\alpha_{ew})$ EW relative correction to the $\gamma\gamma \rightarrow \tilde{\tau}_2\tilde{\tau}_2$ subprocess. The solid, dashed, dotted and dash-dotted curves correspond to four different data set cases, respectively.

Figure 6(a) The Born and full $\mathcal{O}(\alpha_{ew})$ EW corrected cross sections for the $\gamma\gamma \rightarrow \tilde{t}_1\tilde{t}_1$ subprocess as the functions of c.m.s. energy of $\gamma\gamma$ collider $\sqrt{\hat{s}}$ with four different data sets, respectively.

Figure 6(b) The full $\mathcal{O}(\alpha_{ew})$ EW relative correction to $\gamma\gamma \rightarrow \tilde{t}_1\tilde{t}_1$ subprocess. Four different curves correspond to four different data sets, respectively.

Figure 6(c) The Born and full $\mathcal{O}(\alpha_s)$ QCD corrected cross sections for the $\gamma\gamma \rightarrow \tilde{t}_1\tilde{t}_1$ subprocess as the functions of c.m.s. energy of $\gamma\gamma$ collider $\sqrt{\hat{s}}$ with four different data sets, respectively.

Figure 6(d) The full $\mathcal{O}(\alpha_s)$ QCD relative correction to $\gamma\gamma \rightarrow \tilde{t}_1\tilde{t}_1$ subprocess.

Figure 7(a) The Born and full $\mathcal{O}(\alpha_{ew})$ EW corrected cross sections for the $\gamma\gamma \rightarrow \tilde{t}_2\tilde{t}_2$ subprocess as the functions of c.m.s. energy of $\gamma\gamma$ collider $\sqrt{\hat{s}}$ with four different data sets, respectively.

Figure 7(b) The full $\mathcal{O}(\alpha_{ew})$ EW relative correction to $\gamma\gamma \rightarrow \tilde{t}_2\tilde{t}_2$ subprocess. Four different curves correspond to four different data sets, respectively.

Figure 7(c) The Born and full $\mathcal{O}(\alpha_s)$ QCD corrected cross sections for the $\gamma\gamma \rightarrow \tilde{t}_2\tilde{t}_2$ subprocess as the functions of c.m.s. energy of $\gamma\gamma$ collider $\sqrt{\hat{s}}$ with four different data sets, respectively.

Figure 7(d) The full $\mathcal{O}(\alpha_s)$ QCD relative correction to $\gamma\gamma \rightarrow \tilde{t}_2\tilde{t}_2$ subprocess.

Figure 8(a) The Born and full $\mathcal{O}(\alpha_{ew})$ EW corrected cross sections for the $\gamma\gamma \rightarrow \tilde{b}_1\tilde{b}_1$ subprocess as the functions of c.m.s. energy $\sqrt{\hat{s}}$ with four data sets, respectively.

Figure 8(b) The full one-loop $\mathcal{O}(\alpha_{ew})$ EW relative correction to $\gamma\gamma \rightarrow \tilde{b}_1\tilde{b}_1$ subprocess.

Figure 8(c) The Born and full $\mathcal{O}(\alpha_s)$ QCD corrected cross sections for the $\gamma\gamma \rightarrow \tilde{b}_1\tilde{b}_1$ subprocess as the functions of c.m.s. energy $\sqrt{\hat{s}}$ with four data sets, respectively.

Figure 8(d) The full $\mathcal{O}(\alpha_s)$ QCD relative correction to $\gamma\gamma \rightarrow \tilde{b}_1\tilde{b}_1$ subprocess.

Figure 9(a) The Born and full $\mathcal{O}(\alpha_{ew})$ EW corrected cross sections for the $\gamma\gamma \rightarrow \tilde{b}_2\tilde{b}_2$ subprocess as the functions of c.m.s. energy $\sqrt{\hat{s}}$ with four data sets, respectively.

Figure 9(b) The full $\mathcal{O}(\alpha_{ew})$ EW relative corrections to $\gamma\gamma \rightarrow \tilde{b}_2\tilde{b}_2$ subprocess.

Figure 9(c) The Born and full $\mathcal{O}(\alpha_s)$ QCD corrected cross sections for the $\gamma\gamma \rightarrow \tilde{b}_2\tilde{b}_2$ subprocess as the functions of c.m.s. energy $\sqrt{\hat{s}}$ with four data sets, respectively.

Figure 9(d) The full $\mathcal{O}(\alpha_s)$ QCD relative correction to $\gamma\gamma \rightarrow \tilde{b}_2\tilde{b}_2$ subprocess.

Figure 10(a) The Born and full $\mathcal{O}(\alpha_{ew})$ EW corrected cross sections for the $e^+e^- \rightarrow \gamma\gamma \rightarrow \tilde{\tau}_1\tilde{\tau}_1$ process as functions of the soft-breaking sfermion mass M_{SUSY} with $\sqrt{s} = 500$

GeV, 800GeV, 1000 GeV, 2000 GeV, respectively.

Figure 10(b) The full $\mathcal{O}(\alpha_{ew})$ EW relative corrections to the $e^+e^- \rightarrow \gamma\gamma \rightarrow \tilde{\tau}_1\bar{\tilde{\tau}}_1$ process as the functions of M_{SUSY} with $\sqrt{s} = 500$ GeV, 800 GeV, 1000 GeV, 2000 GeV, respectively.

Figure 10(c) The Born and full $\mathcal{O}(\alpha_{ew})$ EW corrected cross sections for the $e^+e^- \rightarrow \gamma\gamma \rightarrow \tilde{\tau}_2\bar{\tilde{\tau}}_2$ process as functions of the soft-breaking sfermion mass M_{SUSY} with $\sqrt{s} = 500$ GeV, 800GeV, 1000 GeV, 2000 GeV, respectively.

Figure 10(d) The full $\mathcal{O}(\alpha_{ew})$ EW relative corrections to the $e^+e^- \rightarrow \gamma\gamma \rightarrow \tilde{\tau}_2\bar{\tilde{\tau}}_2$ process as the functions of M_{SUSY} with $\sqrt{s} = 500$ GeV, 800 GeV, 1000 GeV, 2000 GeV, respectively.

Figure 11(a) The Born and full $\mathcal{O}(\alpha_{ew})$ EW corrected cross sections for the $e^+e^- \rightarrow \gamma\gamma \rightarrow \tilde{t}_1\bar{\tilde{t}}_1$ process as the functions of the soft-breaking sfermion mass M_{SUSY} with $\sqrt{s} = 500, 800, 1000, 2000$ GeV, respectively.

Figure 11(b) The full $\mathcal{O}(\alpha_{ew})$ EW relative corrections to the $e^+e^- \rightarrow \gamma\gamma \rightarrow \tilde{t}_1\bar{\tilde{t}}_1$ process as the functions of M_{SUSY} with $\sqrt{s} = 500$ GeV, 800 GeV, 1000 GeV, 2000 GeV, respectively.

Figure 11(c) The Born and full $\mathcal{O}(\alpha_s)$ QCD corrected cross sections for the $e^+e^- \rightarrow \gamma\gamma \rightarrow \tilde{t}_1\bar{\tilde{t}}_1$ process as the functions of the soft-breaking sfermion mass M_{SUSY} with $\sqrt{s} = 500, 800, 1000, 2000$ GeV, respectively.

Figure 11(d) The full $\mathcal{O}(\alpha_s)$ QCD relative corrections to the $e^+e^- \rightarrow \gamma\gamma \rightarrow \tilde{t}_1\bar{\tilde{t}}_1$ process as the functions of M_{SUSY} with $\sqrt{s} = 500$ GeV, 800 GeV, 1000 GeV, 2000 GeV, respectively.

Figure 12(a) The Born and full $\mathcal{O}(\alpha_{ew})$ EW corrected cross sections for the $e^+e^- \rightarrow \gamma\gamma \rightarrow \tilde{t}_2\bar{\tilde{t}}_2$ process as the functions of the soft-breaking sfermion mass M_{SUSY} with $\sqrt{s} = 1000$ GeV, 2000 GeV, respectively.

Figure 12(b) The full $\mathcal{O}(\alpha_{ew})$ EW relative corrections to the $e^+e^- \rightarrow \gamma\gamma \rightarrow \tilde{t}_2\bar{\tilde{t}}_2$ process as the functions of M_{SUSY} with $\sqrt{s} = 1000$ GeV, 2000 GeV, respectively.

Figure 12(c) The Born and full $\mathcal{O}(\alpha_s)$ QCD corrected cross sections for the $e^+e^- \rightarrow \gamma\gamma \rightarrow \tilde{t}_2\bar{\tilde{t}}_2$ process as the functions of the soft-breaking sfermion mass M_{SUSY} with $\sqrt{s} = 1000$ GeV, 2000 GeV, respectively.

Figure 12(d) The full $\mathcal{O}(\alpha_s)$ QCD relative corrections to the $e^+e^- \rightarrow \gamma\gamma \rightarrow \tilde{t}_2\bar{\tilde{t}}_2$ process as the functions of M_{SUSY} with $\sqrt{s} = 1000$ GeV, 2000 GeV, respectively.

Figure 13(a) The Born and full $\mathcal{O}(\alpha_{ew})$ EW corrected cross sections for the $e^+e^- \rightarrow \gamma\gamma \rightarrow \tilde{b}_1\bar{\tilde{b}}_1$ process as the functions of the soft-breaking sfermion mass M_{SUSY} with $\sqrt{s} = 500$ GeV, 800 GeV, 1000 GeV, 2000 GeV, respectively.

Figure 13(b) The full $\mathcal{O}(\alpha_{ew})$ EW relative corrections to the $e^+e^- \rightarrow \gamma\gamma \rightarrow \tilde{b}_1\bar{\tilde{b}}_1$ process as the functions of M_{SUSY} with $\sqrt{s} = 500$ GeV, 800 GeV, 1000 GeV, 2000 GeV, respectively.

Figure 13(c) The Born and full $\mathcal{O}(\alpha_s)$ QCD corrected cross sections for the $e^+e^- \rightarrow \gamma\gamma \rightarrow \tilde{b}_1\bar{\tilde{b}}_1$ process as the functions of the soft-breaking sfermion mass M_{SUSY} with $\sqrt{s} = 500$ GeV, 800 GeV, 1000 GeV, 2000 GeV, respectively.

Figure 13(d) The full $\mathcal{O}(\alpha_s)$ QCD relative corrections to the $e^+e^- \rightarrow \gamma\gamma \rightarrow \tilde{b}_1\bar{\tilde{b}}_1$ process as the functions of M_{SUSY} with $\sqrt{s} = 500$ GeV, 800 GeV, 1000 GeV, 2000 GeV, respectively.

Figure 14(a) The Born and full $\mathcal{O}(\alpha_{ew})$ EW corrected cross sections for the $e^+e^- \rightarrow \gamma\gamma \rightarrow \tilde{b}_2\bar{\tilde{b}}_2$ process as the functions of the soft-breaking sfermion mass M_{SUSY} with $\sqrt{s} = 800$ GeV, 1000 GeV, 2000 GeV, respectively.

Figure 14(b) The full $\mathcal{O}(\alpha_{ew})$ EW relative corrections to the $e^+e^- \rightarrow \gamma\gamma \rightarrow \tilde{b}_2\bar{\tilde{b}}_2$ process as the functions of M_{SUSY} with $\sqrt{s} = 800$ GeV, 1000 GeV, 2000 GeV, respectively.

Figure 14(c) The Born and full $\mathcal{O}(\alpha_s)$ QCD corrected cross sections for the $e^+e^- \rightarrow$

$\gamma\gamma \rightarrow \tilde{b}_2\bar{\tilde{b}}_2$ process as the functions of the soft-breaking sfermion mass M_{SUSY} with $\sqrt{s} = 800$ GeV, 1000 GeV, 2000 GeV, respectively.

Figure 14(d) The full $\mathcal{O}(\alpha_s)$ QCD relative corrections to the $e^+e^- \rightarrow \gamma\gamma \rightarrow \tilde{b}_2\bar{\tilde{b}}_2$ process as the functions of M_{SUSY} with $\sqrt{s} = 800$ GeV, 1000 GeV, 2000 GeV, respectively.